2015

Theoretical And Experimental Investigation Of The Cascading Nature Of Pressure-Swirl Atomization

Pretam Choudhury
University of Central Florida

THEORETICAL AND EXPERIMENTAL INVESTIGATION OF THE CASCADING NATURE OF PRESSURE-SWIRL ATOMIZATION

by

PRETAM K. CHOUDHURY
B.S. Georgia Institute of Technology, 2010

A thesis submitted in partial fulfilment of the requirements
for the degree of Master of Science in Mechanical Engineering
in the Department of Mechanical and Aerospace Engineering
in the College of Engineering and Computer Science
at the University of Central Florida
Orlando, Florida

Spring Term
2015

ABSTRACT

Pressure swirl atomizers are commonly used in IC, aero-engines, and liquid propellant rocket combustion. Understanding the atomization process is important in order to enhance vaporization, mitigate soot formation, design of combustion chambers, and improve overall combustion efficiency. This work utilizes non-invasive techniques such as ultra -speed imaging, and Phase Doppler Particle Anemometry (PDPA) in order to investigate the cascade atomization process of pressure-swirl atomizers by examining swirling liquid film dynamics and the localized droplet characteristics of the resulting hollow cone spray. Specifically, experiments were conducted to examine these effects for three different nozzles with orifice diameters .3mm, .5mm, and .97mm.

The ultra-speed imaging allowed for both visualization and interface tracking of the swirling conical film which emanated from each nozzle. Moreover, this allowed for the measurement of the radial fluctuations, film length, cone angle and maximum wavelength. Radial fluctuations are found to be maximum near the breakup or rupture of a swirling film. Film length decreases as Reynolds number increases. Cone angle increases until a critical Reynolds number is reached, beyond which it remains constant.

A new approach to analyze the temporally unstable waves was developed and compared with the measured maximum wavelengths. The new approach incorporates the attenuation of a film thickness, as the radius of a conical film expands, with the classical dispersion relationship for an inviscid moving liquid film. This approach produces a new long wave solution which accurately matches the measured maximum wavelength swirling conical films generated from nozzles with the smallest orifice diameter. For the nozzle with the largest orifice diameter, the new long wave solution provides the upper bound limit, while the long wave solution for a constant film thickness provides the lower bound limit. These results indicate that temporal instability is the dominating

mechanism which generates long Kelvin Helmholtz waves on the surface of a swirling liquid film.

The PDPA was used to measure droplet size and velocity in both the near field and far field of the spray. For a constant Reynolds number, an increase in orifice diameter is shown to increase the overall diameter distribution of the spray. In addition, it was found that the probability of breakup, near the axis, decreases for the largest orifice diameter. This is in agreement with the cascading nature of atomization.

"We choose to go to the moon in this decade and do the other things, not because they are easy, but because they are hard, because that goal will serve to organize and measure the best of our energies and skills, because that challenge is one that we are willing to accept, one we are unwilling to postpone, and one which we intend to win, and the others, too." - John F. Kennedy

ACKNOWLEDGMENTS

I would like to express my gratitude to my advisor, Dr. Ranganathan Kumar, for his support and guidance throughout my graduate career. You allowed me to explore new fields and discover new interests in the unexplored areas of fluid dynamics. Additionally, I would like to express my gratitude to my committee members, Dr. Hansen Mansy and Dr. Weiwei Deng. Your genuine help and thoughtful discussions allowed to me to complete my thesis and enhance my academic knowledge.

Also, I would like to thank my colleagues, Dr. Joshua Lee, Ashkan Davanlou, James Wilson, Eduardo Castillo, Kalpana Madhushan, Richard Stadelmann, Anthony Terriciano, Najat Hamri, Majid Haghshenas, and Carlos Velez. Each one of you have astonishing skills and invaluable traits which humbles me to know that I had the chance to work with all of you. I am much obliged for the help I recieved from all of you. But more importantly, I am forever grateful for the belief and confidence you all have instilled in me. All of you have believed in me; even during times when I did not believe in myself. There were many times where I felt I was progressing fast with null results, yet you all encouraged me 'to do the hard thing', to keep discovering. For this reason, I will always march forward along side each one of you, even in the most hopeless of situations.

Lastly, I would like to acknowledge those who have I have often neglected, but have never forgotten. I would like to thank my father Pijush, my mother Shikha, my sister Samantha, my trusted friends, Ryan, Napoleon, Edgar and Alex. Regardless of how preoccupided I become, you all have went out of your way to interact with me, to help me, to empathize and even sympathize with me when I did not deserve it. All of you have done more for me than I have ever done for you. It is truly my unremitting regret that I will never be able to return the favor. Nevertheless, I thank you and I am glad to know that you are by my side.

TABLE OF CONTENTS

LIST OF FIGURES

LIST OF TABLES

CHAPTER 1: INTRODUCTION

1.1 Pressure-Swirl Atomizers

Pressure-swirl atomizers are commonly used in IC, aero-engines and liquid propellant rocket combustion. Pressure-swirl atomizers allow for the atomization of high volume fuel flows into micron sized droplets. This is beneficial because it is shown that smaller droplet sizes lead reduced vaporization time.

Therefore,the droplet size profile is of high interest. However, the droplet size profile is influenced by many factors such as the flow field characteristics, droplet-droplet interactions. In total, all these factors can be grouped together into one phenomena: the cascading nature of pressure-swirl atomization.

1.2 Cascade Atomization

Cascade atomization in general is a complex phenomenon which includes many breakup processes which occur sequentially or sometimes even simultaneously. For instance, a velocity discontinuity between the interface of an ambient environment and thin liquid film may cause unstable surface waves to grow on the surface of the liquid film and lead to the breakup of the liquid film into ligaments. The subsequently formed ligaments are then subject to unstable surface deformations caused by pressure fluctuations, which lead to the formation of droplets. Additionally, the droplets can be subject to either aerodynamic force or pressure fluctuations and breakup into daughter droplets as shown in figure 1.1. In the particular scenario of pressure-swirl atomization, it is shown that all these instabilities not only occur during the cascade atomization process, but occur at different sequences or at different flow regimes.

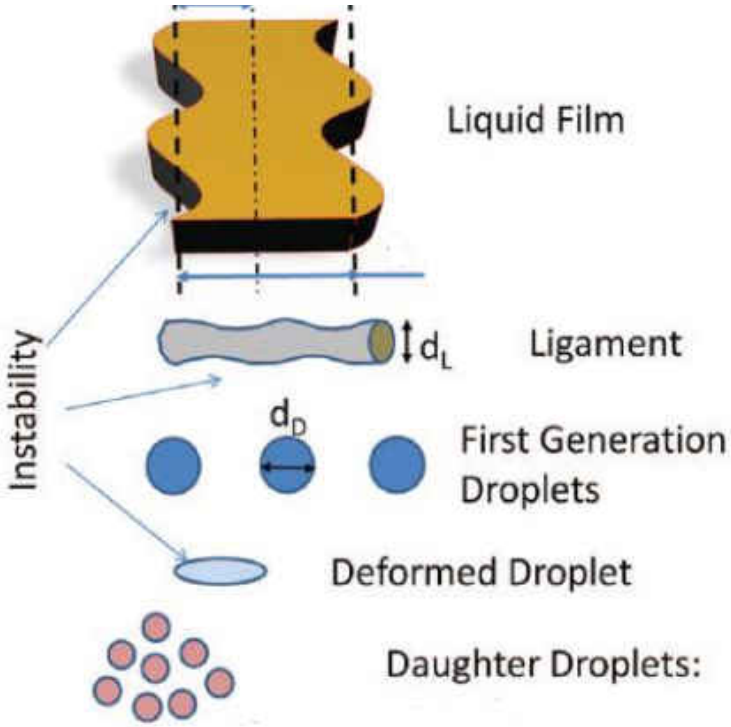

Figure 1.1: Cascade atomization process for a thin film. The liquid film undergoes a sequence of breakup processes which lead to the formation of droplets. Each of these breakup processes are governed by a hydrodynamic instability. Adapted from Saha et al. (2012)

The individual breakup processes are governed by a form of hydrodynamic instability. Some hydrodynamic instabilities which occur during the cascade phenomenon are Rayleigh Taylor Instability(RTI), Kelvin Helmholtz instability(KHI), and Rayleigh Plateau Instability(RPI). RTI primarily occurs due to one fluid accelerating and penetrating another fluid with a different density. This penetration causes the formation of a mushroom-shaped head as shown in figure 1.2 (a). KHI primarily occurs due to unstable wave growth on a liquid interface of two fluids with different velocities. Wave formation is indicative of KHI as shown in figure 1.2 (b). RPI primarily occurs due to pressure fluctuations imposed in a liquid, with unstable curvature, by surface tension. RPI is often accompanied with a 'pinch off' mechanism as shown in figure 1.2 (c).

Figure 1.2: (a)Morphology of RTI. Adapted from Kull(1991). (b) Morphology of KHI. Adapted from Rangel and Sirignano(1988). (c) Morphology of RPI. Adapted from Eggers and Villermaux(2008).

In the particular scenario of pressure-swirl atomization, it is shown that all these instabilities not only occur during the cascade atomization process, but occur at different sequences or in different flow regimes. This unique behavior demonstrates the complexity of the cascading nature of pressure-swirl atomization. In order to take the first step in understanding this phenomenon, the fundamental physics of liquid sheet atomization must first be discussed.

1.3 Literature Search In Thin Sheet Atomization

Atomization is a process consisting of linear and non-linear wave instabilities which induce breakup of a continuous fluid phase. Therefore to understand the atomization process, the type of waves which propagate within the dense fluid of a spray must be evaluated.

1.3.1 Dispersive Waves in a Dense Fluid

Rayleigh (1899) and Plateau(1873) were one of the first to discover that waves propagating on the surface of an incompressible fluid are dispersive in nature. Dispersive waves are unique in that they are characterized by the solution of a governing equation. Essentially a dispersive wave has the typical form

$$\xi = \xi_0 e^{ikx - i\omega t} \tag{1.1}$$

where k is the wave number, ω is the angular frequency, and ξ_0 is the amplitude. It should be noted that if the solution to ξ is separable, then the amplitude can be described as an oscillatory function $\xi_0(kx)$. From equation 1.1 it is apparent that there is a coupled behavior between ω and k, such that

$$\omega = \omega(k) \tag{1.2}$$

Equation 1.2 is often referred to as the dispersion relationship. The significance of the dispersion relationship is that a wave's frequency is dependant upon the wave number.

For linear dispersions a more general form can be made with the use of Fourier integrals as

$$\xi = \int_{-\infty}^{\infty} F(k) e^{kx - \omega(k)t} dk \tag{1.3}$$

From equation 1.3 the phase speed can be obtained as $c(k) = \frac{\omega(k)}{k}$. However, dispersive waves are such that each wave in a wave train will have a different phase speed if the wave number(or wavelength) of a given wave is different from the companion waves. Essentially the wave train is considered an oscillatory train, where the amplitude fluctuates as a wave coalesces or travels past another wave. Therefore in terms of examining propagation of a wave train, the group velocity provides a more suitable interpretation of propagation.

$$c_g = \frac{\mathrm{d}\omega}{\mathrm{d}k} \tag{1.4}$$

Equation 1.4 is a powerful interpretation which can be used to described energy propagation or amplification (see section 3.3).

1.3.2 Short Wave and Long Wave Interpretation

Often the dispersion relationship displays behavior which is difficult to observe any tendencies. Therefore it is useful to use asymptotic analysis to observe the dispersion relationship for either asymptotically long wavelength(small argument for k) or or asymptotically short wavelength(large argument for k).

In order to simplify the dispersion relationship for long wavelength or short wavelength interpretation, $\omega(k)$ must be asymptotically expanded for both small k and large k, respectfully.

For long wavelength, $\omega(k)$ should be a form comparable to:

$$\omega(k) = K_0 + K_1 k + K_2 k^2 + K_3 k^3 + \mathcal{O}(k^4) \tag{1.5}$$

For short wavelength, $\omega(k)$ should be a form comparable to:

$$\omega(k) = L_{-1} k + L_0 + L_1 \frac{1}{k} + L_2 \frac{1}{k^2} + L_3 \frac{1}{k^3} + \mathcal{O}\left(\frac{1}{k^4}\right) \tag{1.6}$$

A few methods for obtaining long wavelength and short wavelength interpretations are regular perturbation expansion, and method of dominant balance. However, there are only a few unique solutions which contain both a short wavelength and long wavelength interpretation. Some of these unique solutions are hyperbolic functions and Bessel functions. If the dispersion relationship contains a combination of hyperbolic functions and/or Bessel functions, then the long wavelength and short wavelength interpretation can be found by simply substituting the respective function with its long wavelength or short wavelength approximation.

Table 1.1: Long and Short wavelength interpretations for hyperbolic tan,modified Bessel function of the first kind, and modified Bessel function of the second kind.

Function	Long Wavelength Interpretation	Short Wavelength Interpretation
$\tanh k$	$k + \mathcal{O}(k^3)$	$1 + \mathcal{O}\left(e^{-2k}\right)$ *or* $1 + o\left(\frac{1}{k}\right)$
$I_0(k)$	$1 + \mathcal{O}(k^2)$	$\frac{e^k}{\sqrt{2\pi k}} + \mathcal{O}\left(\frac{1}{k^{3/2}}\right)$
$I_1(k)$	$\frac{k}{2} + \mathcal{O}(k^3)$	$\frac{e^k}{\sqrt{2\pi k}} + \mathcal{O}\left(\frac{1}{k^{3/2}}\right)$
$K_0(k)$	$\sim -\ln k$	$\sqrt{\frac{\pi}{2k}} e^{-k} + \mathcal{O}\left(\frac{e^{-k}}{k^{3/2}}\right)$ *or* $\sqrt{\frac{\pi}{2k}} e^{-k} + o\left(\frac{1}{k^{3/2}}\right)$
$K_1(k)$	$\frac{1}{k} + \mathcal{O}(k)$	$\sqrt{\frac{\pi}{2k}} e^{-k} + \mathcal{O}\left(\frac{e^{-k}}{k^{3/2}}\right)$ *or* $\sqrt{\frac{\pi}{2k}} e^{-k} + o\left(\frac{1}{k^{3/2}}\right)$

1.3.3 Linear Stability Analysis

Identifying instability in nonlinear solutions is quite difficult. Often instability is only recognized simply because the solution shows irregular behavior. However, in linear solutions, instability can be determined from the growth rate of the dependant variable.

For instance, lets examine the first order ordinary differential system shown below.

$$\dot{\boldsymbol{x}} = \boldsymbol{A}\boldsymbol{x} \tag{1.7}$$

Where $\dot{\boldsymbol{x}}$ and $\boldsymbol{x}$ are mxn matrices and $\boldsymbol{A}$ is a mxm matrix. While this system can be solved for an exact solution, lets assume it cannot and expand $\boldsymbol{x}$ by a small parameter ϵ.

$$\boldsymbol{x}(t) = \boldsymbol{x_0} + \varepsilon \boldsymbol{x_1} + \mathcal{O}(\varepsilon^2) \tag{1.8}$$

$$or$$

$$\boldsymbol{x}(t) \sim \boldsymbol{x_0} + \Delta \boldsymbol{x} \tag{1.9}$$

Where $\boldsymbol{x_0}$ is independent of t and $\Delta \boldsymbol{x}$ is a small perturbation. The first order system now looks like this.

$$\dot{\boldsymbol{x}} = \Delta \dot{\boldsymbol{x}} \tag{1.10}$$

$$\Delta \dot{\boldsymbol{x}} = \boldsymbol{A}\Delta \boldsymbol{x} + \boldsymbol{A}\boldsymbol{x_0} \tag{1.11}$$

Solving for the homogeneous equation, the solution is:

$$\Delta \boldsymbol{x} = \vec{v} e^{\lambda_m t} \tag{1.12}$$

If $\lambda_m > 0$ then the small perturbation $\Delta \boldsymbol{x}$ would grow exponentially large. If that is the case than the solution would violate the definition. In other words the solution becomes unstable.

Now lets assume the small perturbation $\Delta \boldsymbol{\xi}$ represents the signal response of a wave train such that:

$$\Delta \boldsymbol{\xi} = \boldsymbol{\xi_0} e^{ikx - i\omega t} \tag{1.13}$$

$$or$$

$$\Delta \boldsymbol{\xi} = \boldsymbol{G}(x) e^{-i\omega t} \tag{1.14}$$

Additionally, ω can be decomposed into a real and imaginary part , $\omega = \omega_r + i\omega_i$. Hence:

$$\Delta \boldsymbol{\xi} = \boldsymbol{G}(x) e^{-i\omega_r t + \omega_i t} \tag{1.15}$$

$$therefore$$

$$\lambda_m = -i\omega_r + \omega_i \tag{1.16}$$

It should be noted that the real component never becomes imaginary unless the wave number is imaginary. Therefore in order for the wave train to exhibit unstable growth $Re(\omega_i) > 0$. Hence, ω_i is termed the growth rate.

While the example shown above is impractical, the underlying principle holds true. This will be shown in the upcoming sections.

1.3.4 Thin Liquid Sheet moving in Ambient Air

Thin liquid sheet moving in ambient air is a classical problem which gives insight into the atomization process for a liquid sheet(Squire 1953, Hagerty and Shea 1955, and Clark and Dombrowski 1972). Because of the density and velocity discontinuity, the thin liquid sheet is subject to Kelvin Helmholtz instability. Kelvin Helmholtz instability manifests itself as growing surfaces waves which ultimately causes the sheet to breakup in wavelength increments. Alternatively, this type of atomization is called wave disintegration.

1.3.5 Two Phase Flow Interpretation

In two phase flow, the phases are separated such that one is considered a continuous phase and the other phase is considered a dispersed phase. For this problem statement, the liquid sheet is the dispersed phase moving at a constant velocity U_0 and the ambient air is the continuous phase. The notation g will indicate the continuous phase, while the notation l will indicate the dispersed phase.

The short hand notation for derivatives will be used as shown below. p stands for phase (l or g).

$$\left.\frac{\partial \Xi}{\partial x}\right|_p = \Xi_{p,x} \tag{1.17}$$

$$\left.\frac{\partial^2 \Xi}{\partial x^2}\right|_p = \Xi_{p,xx} \tag{1.18}$$

1.3.6 Problem statement

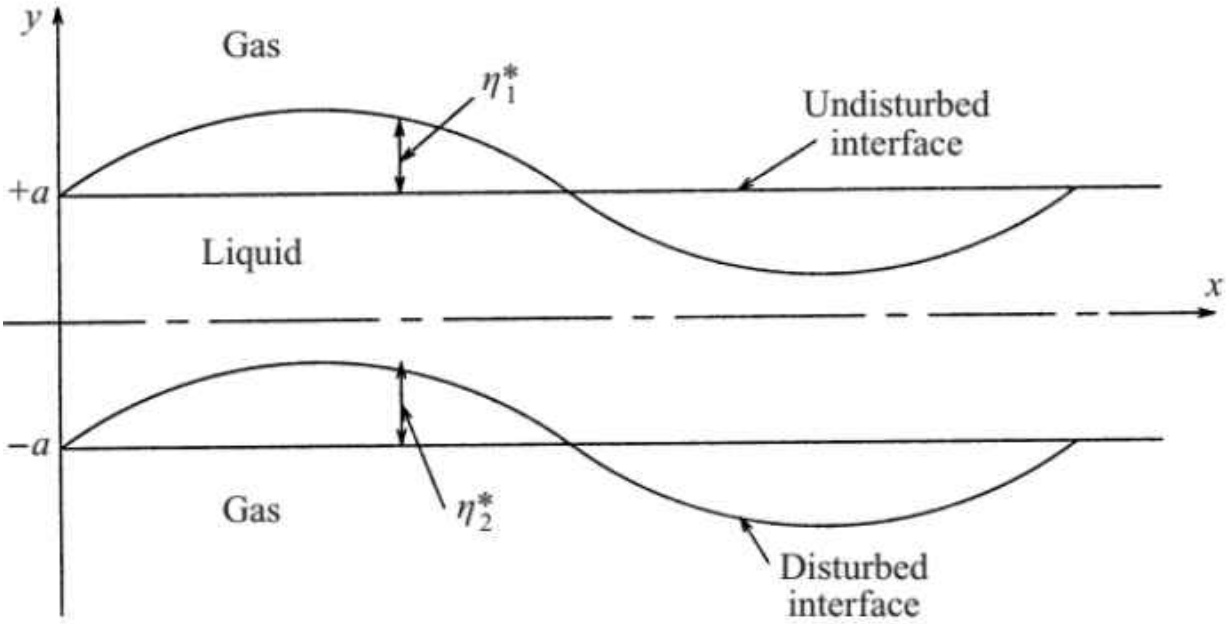

Figure 1.3: Nonlinear instability of a plane liquid sheet(Jazayeri and Li 2000). It should be noted for the current problem statement $h_0 = 2a$.

The thin liquid sheet is moving with a constant velocity U_0 and has an undisturbed film thickness h_0. Additionally, the interface is deflected by some η.

1.3.6.1 Governing Equation

The governing equation is the continuity equation is nondimensionlized as $u = \frac{u^*}{U_0}$,$v = \frac{v^*}{U_0}$, $t = \frac{t^* U_0}{h_0}$, $x = \frac{x^*}{h_0}$, and $y = \frac{y^*}{h_0/2}$.

$$u_{g,x} + v_{g,y} = 0 \tag{1.19}$$

$$u_{l,x} + v_{l,y} = 0 \tag{1.20}$$

Under the assumption of inviscid and irrotational flow, the governing equations can be further simplified as such.

$$\phi_{g,xx} + \phi_{g,yy} = 0 \tag{1.21}$$

$$\phi_{l,xx} + \phi_{l,yy} = 0 \tag{1.22}$$

1.3.6.2 Boundary Conditions

Using the free surface condition at the interface $y = \pm 1$, the kinematic boundary condition is obtained.

$$\phi_{l,y} - \eta_{j,t} - \phi_{l,x}\eta_{j,x} = 0 \tag{1.23}$$

$$\phi_{g,y} - \eta_{j,t} - \phi_{g,x}\eta_{j,x} = 0 \tag{1.24}$$

Where $j = \pm 1$ which represents either the upper or lower interface.

Given that the curvature of the interface is defined as $f(x, y) = 1 + (-1)^(j)\eta_j$, the normal to the interface can be found as $n = \frac{\nabla f}{|\nabla f|}$. Moreover the laplace equation can be obtained.

$$\nabla \cdot n = \frac{(-1)^j \eta_{j,xx}}{(1 + \eta_{j,x}^2)^{3/2}} \tag{1.25}$$

$$P_g - P_l = \frac{(-1)^j}{We_s} \frac{\eta_{j,xx}}{(1 + \eta_{j,x}^2)^{3/2}} \tag{1.26}$$

Where $P = \frac{P^* h_0}{\sigma}$ and $We_s = \frac{\rho_l U_0^2 h_0}{\sigma}$. Using the Bernoulli equation to solve for both pressures, the dynamic boundary condition can be determined as shown below.

$$Q\phi_{g,t} - \phi_{l,t} + \frac{1}{2}Q(\phi_{g,x}^2 + \phi_{g,y}^2) - \frac{1}{2}(\phi_{l,x}^2 + \phi_{l,y}^2) = \frac{(-1)^j}{We_s} \frac{\eta_{j,xx}}{(1 + \eta_{j,x}^2)^{3/2}} \tag{1.27}$$

1.3.6.3 Regular expansion

The three main quantities $\eta_j,\ \phi_l,\ \phi_g$ can be expanded about a small parameter ϵ. Note that ϵ is an artificial parameter, therefore can mean anything. For this study and also done in the work of Jazayeri and Li(2000), ϵ will be taken as the ratio of the disturbance amplitude to initial amplitude.

$$\eta_j = \sum_{n=1}^{\infty} \varepsilon^n \eta_{jn}(x,t) \tag{1.28}$$

$$\phi_l = \sum_{n=0}^{\infty} \varepsilon^n \phi_{ln}(x,y,t) \tag{1.29}$$

$$\phi_g = \sum_{n=0}^{\infty} \varepsilon^n \phi_{gn}(x,y,t) \tag{1.30}$$

1.3.7 First Order Solution $\mathcal{O}(\varepsilon)$:

$$\phi_{g1,xx} + \phi_{g1,yy} = 0 \quad for\ y\ \in\ [1,+\infty)\ \ and\ \ y\ \in\ (-\infty,-1] \tag{1.31}$$

$$\phi_{l1,xx} + \phi_{l1,yy} = 0 \quad for\ y\ \in\ [-1,1] \tag{1.32}$$

$$\phi_{l1,y} - \eta_{j1,t} - \eta_{j1,x} = 0 \tag{1.33}$$

$$\phi_{g1,y} - \eta_{j1,t} = 0 \tag{1.34}$$

$$Q\phi_{g1,t} - \phi_{l1,t} - \phi_{l1,x} - (-1)^j \frac{\eta_{j1,xx}}{We} = 0 \tag{1.35}$$

1.3.7.1 *Linear Solution for Sinuous Mode*

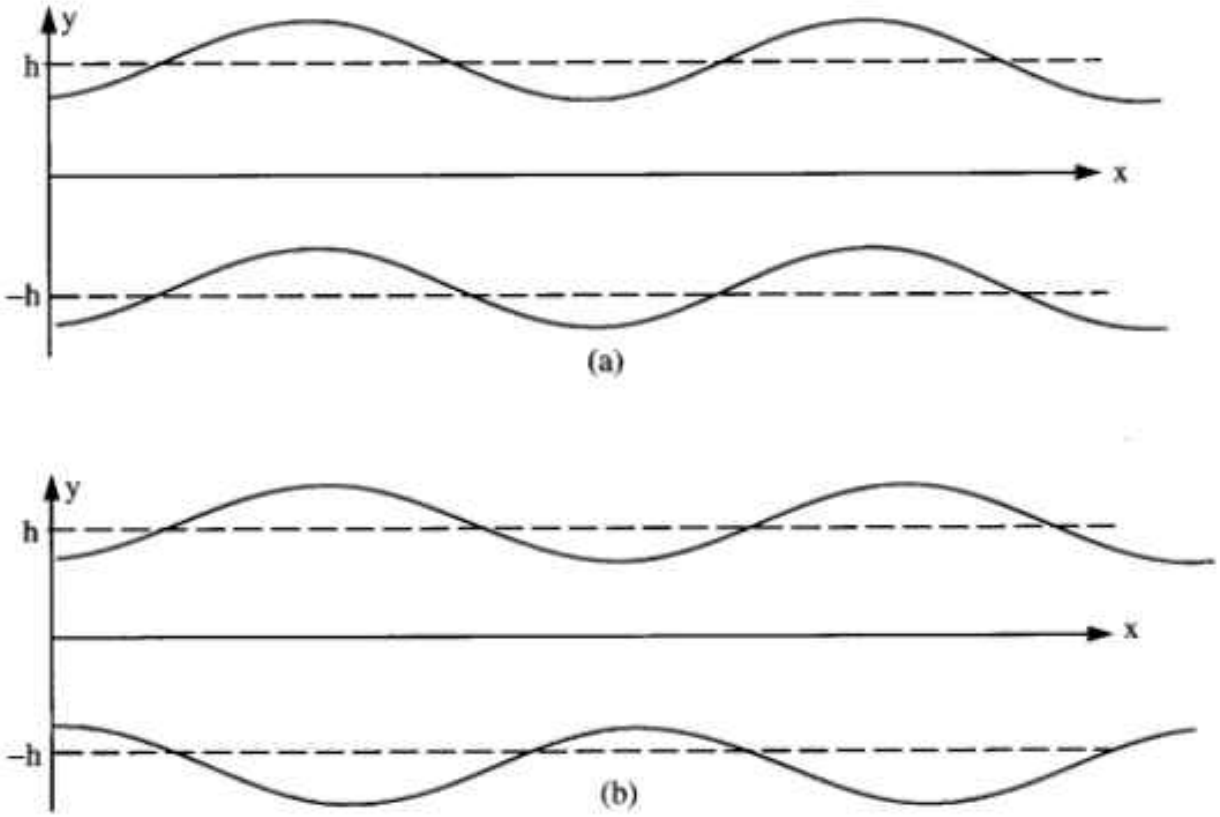

Figure 1.4: Two predominant unstable modes on the interface of a liquid sheet(Senecal et al. 1999). (a) Sinuous mode or antisymmetric mode. (b) Varicose mode, dilation mode, or symmetrical mode. It should be noted for the current problem statement $h_0 = 2h$.

Hagerty and Shea(1955) discovered that the two most predominant modes of instability, found on liquid sheet, were sinuous mode or varicose mode. Moreover, it was shown that sinuous mode tends to have a larger growth rate than varicose mode, for a liquid sheet. Sinuous mode has the form

$$\xi = h_s \cosh kz e^{i(kx-\omega t)} \tag{1.36}$$

All the solutions can take a normal form as shown below.

$$\phi_{l1} = \psi_s \cosh ky e^{i(kx-\omega t)} \tag{1.37}$$

$$\phi_{g1} = \psi_{s2} e^{\mp ky + i(kx-\omega t)} \tag{1.38}$$

$$\eta_{j1} = f e^{i(kx-\omega t)} \tag{1.39}$$

Therefore equations 1.31 - 1.35 above can be solved to yield Squire's solution.

$$Q\omega^2 + (k-\omega)^2 \tanh(k) - k^3 We^{-1} = 0 \tag{1.40}$$

$$\omega_r = -\frac{k \tanh k}{\tanh k + Q} \tag{1.41}$$

$$\omega_i = \pm \frac{k\sqrt{Q \tanh k - (\tanh k + Q)k/We}}{\tanh k + Q} \tag{1.42}$$

Figure 1.5 shows the typical growth rate plot. The growth rate observations, give more insight into the range of unstable wave numbers there are. Also, the maximum value of a growth is used as an indication of where breakup or rupture of a sheet will occur.

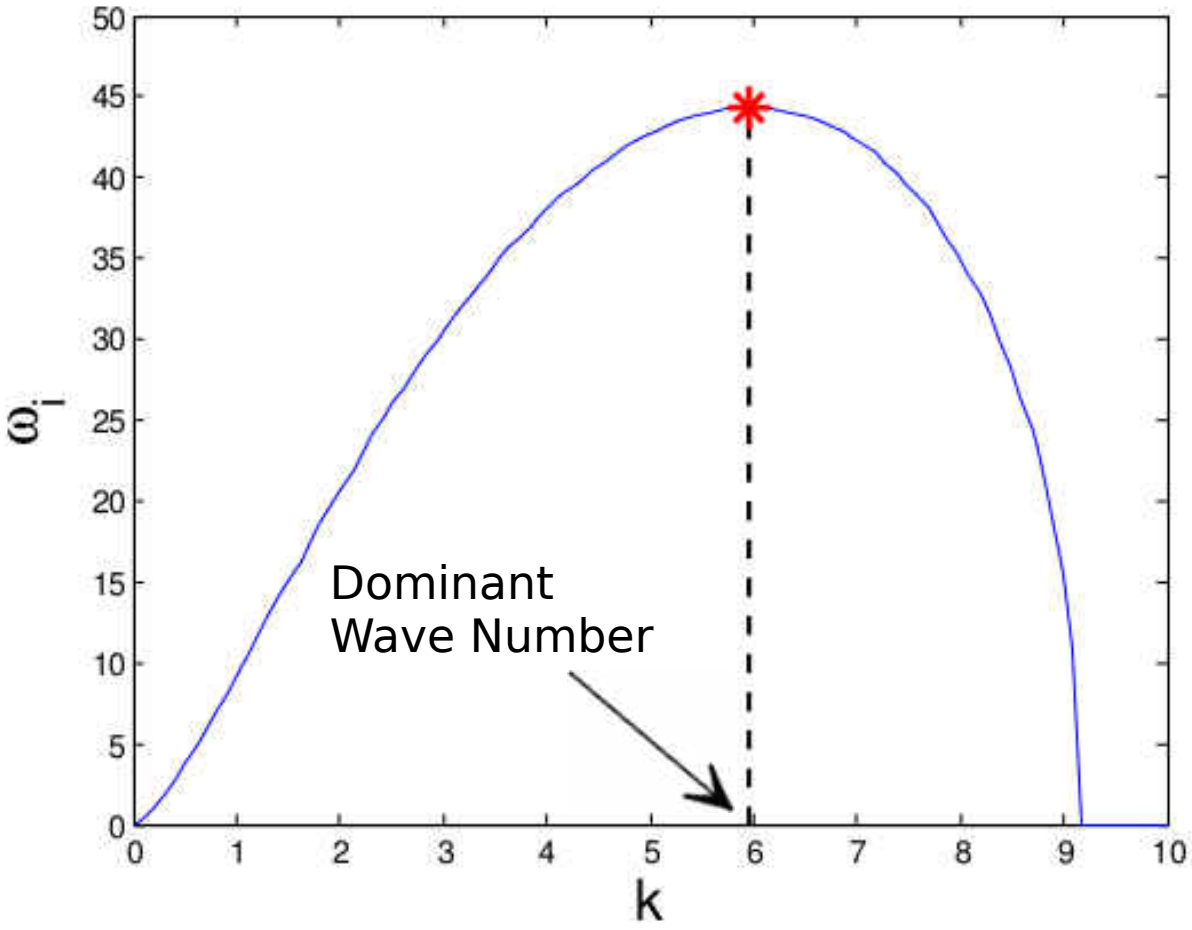

Figure 1.5: Growth rate solved from Squire's solution.

1.3.7.2 Long Wave and Short Wave Interpretation of Squire's solution

From table 1.1 we see that for long wavelength $\tanh k \sim k$ and for short wavelength $\tanh k \sim 1$. This value can be plugged into the dispersion relationship or growth rate to get better insight of the problem.

Long wavelength interpretation of Squire's Results:

$$\omega_i = \frac{k\sqrt{Qk - (k+Q)k/We}}{k+Q} \tag{1.43}$$

Short wavelength interpretation of Squire's Results:

$$\omega_i = \frac{k\sqrt{Q - (1+Q)k/We}}{k+Q} \tag{1.44}$$

While Squire's results are simply enough to solve the entire equation, other dispersion models are not as easy to interpret . Therefore using long wavelength or short wavelength interpretation can be beneficial.

1.3.8 Second Order Solution $\mathcal{O}(\varepsilon^2)$

:

While linear solution allows us to evaluate instability, it does not demonstrate breakup of a liquid sheet. In order to examine breakup of a liquid sheet, the solution must be expanded to atleast a second higher term.

$$\eta_{j2} = \psi_{j2}e^{2ikx} + \overline{\psi}_{j2}e^{-2ikx} \tag{1.45}$$

$$\omega_{2r} = -\frac{2k\coth 2k}{\coth 2k\rho} \tag{1.46}$$

$$\omega_{2i} = \pm\frac{2k\sqrt{\rho\coth 2k - (\coth 2k + \rho)2k/We_h}}{\coth 2k + \rho} \tag{1.47}$$

where the coefficients are given as shown below.

$$\psi_{j2} = (-1)^j \left(A_1 e^{i\omega_2 t} + \overline{A_1} e^{i\overline{\omega}_2 t} + A_2 e^{2i\omega_1 t} + \overline{A_2} e^{2i\overline{\omega}_1 t} + A_3 e^{2i\omega_{2r} t} \right) \tag{1.48}$$

$$A_1 = \frac{C}{(\omega_2 - \overline{\omega}_2)(\omega_2 - 2\overline{\omega}_1)} + \frac{\overline{C}}{(\omega_2 - \overline{\omega}_2)(\omega_2 - 2\omega_1)} + \frac{E}{(\omega_2 - \overline{\omega}_2)(\omega_2 - 2\omega_{2r})} \tag{1.49}$$

$$A_2 = \frac{\overline{C}}{(\overline{\omega}_2 - 2\omega_1)(\omega_2 - 2\omega_1)} \tag{1.50}$$

$$A_3 = \frac{E}{(\overline{\omega}_2 - 2\omega_{1r})(\omega_2 - 2\omega_{1r})} \tag{1.51}$$

$$C = -\frac{1}{32} \left((\tanh k^2 + 4 \coth 2k \tanh k - 5)(\overline{\omega}_1^2 + 2k\overline{\omega}_1 + k^2) \right) \tag{1.52}$$

$$\begin{aligned} E = -\frac{1}{16}((k^2 + 2k\omega_{1r})(\tanh k^2 + 4 \coth 2k \tanh k = 5) \\ + 2(\omega_{1i}^2 + \omega_{1r}^2)(\tanh k \coth 2k + \frac{1/2}{\tanh} k^2 - \frac{3}{2}) \\ - 2(\omega_{1i}^2 - \omega 1 r^2)(\tanh k \coth 2k - 1) - 1) \end{aligned} \tag{1.53}$$

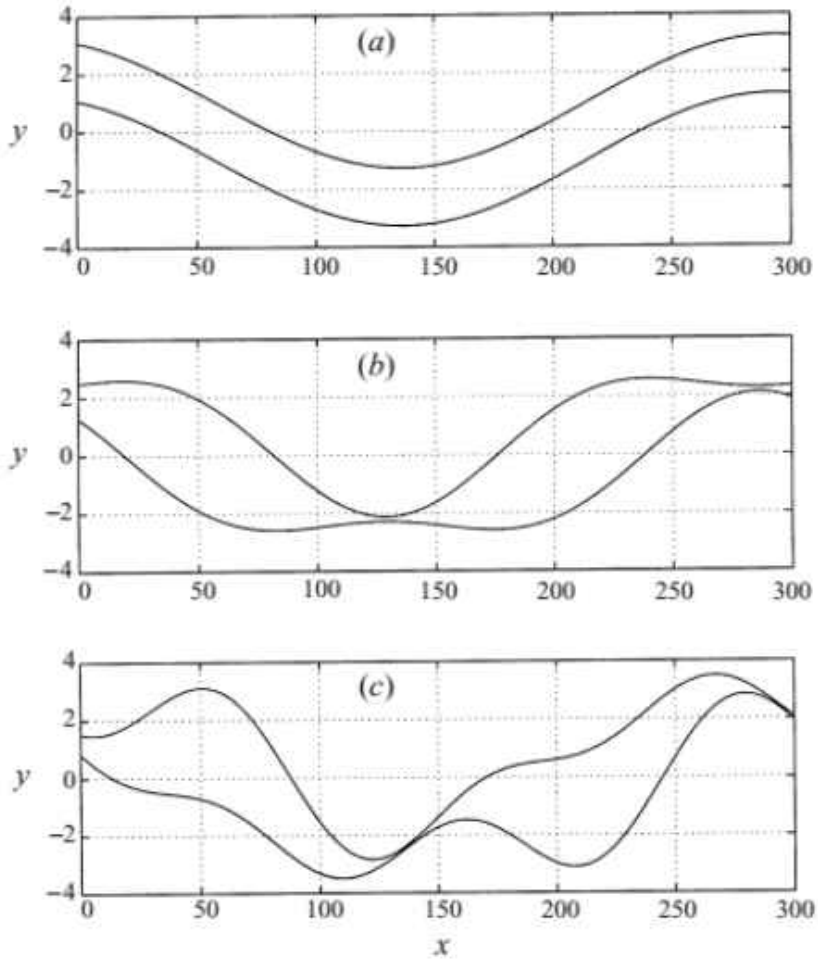

Figure 1.6: The breakup evolution as higher harmonics are introduced to the solution(Jazayeri and Li 2000). (a)Only the first harmonic exists. The solution is linear and sinuous. (b) Second harmonic is introduced and causes pinch off behavior. (c) Third harmonic causes more undulations on the sheet.

Figure 1.6 shows the effect of nonlinearity in the solution. Figure 1.6 (a) shows the linear solution for a unstable k, or $Re(\omega_i) > 0$. While the solution shows large sinuous deformations, it is not necessarily breaking up. However, from figure 1.6 (b) it is observed that a pinch off mechanism is occurring. This is due to the contribution of the second order harmonic which acts as a varicose mode. The second order varicose mode is smaller in magnitude than the fundamental

harmonic. However, the varicose disturbance is 180 degrees out of phase with the fundamental harmonic. Thus, while the interface deforms over a large time, the second harmonic induces pinching which leads to breakup.

This result determined by Jazayeri and Li(2000) is profound. This finding concludes that the breakup of a thin sheet is actually governed by the nonlinear effects which induce varicose disturbances, over a long time. However, does this result hold true for an attenuating sheet, where time scales are much smaller? This will be examined in 3.2.

1.3.9 Influence of Thin Liquid Sheet Atomization in Pressure-Swirl Atomization

Pressure-Swirl atomization is distinctly, different from thin liquid sheet atomization. Two major differences are that in pressure-swirl atomization the sheet is swirling and the film thickness is attenuating. However while these are significant distinctions, these distinctions do not discredit the use of thin liquid sheet atomization theory in the examination of pressure-swirl atomization. In fact, Crapper and Dombrowski (1975) and Mehring and Sirignano (2001) have demonstrated that the dispersion relationship for annular sheet with aerodynamic effects, and annular sheet with swirl effects , respectively can be reduced to the 2-D counterpart if radius is very large or if $\frac{\lambda}{h} \sim 1$. Therefore, under certain criteria 2-D assumption becomes valid. An additional scope of this work is the examination of when 2-D assumption is valid.

1.4 Significance Of This Work

The breadth of this work covers broad aspects of atomization which have been touched upon by previous work. Therefore it is important to distinguish the current work from past work.

Table 1.2: Summary of Past Work and Current Work done within the topic of pressure-swirl atomization.

Contribution	Saha et al. (2012)	Lee et al. (2013)	Current Work
Investigated droplet size and velocity profile	✓	✓	✓
Investigated unstable wavelengths	✓		✓
Investigated coalescence of droplets			✓
Investigated liquid film velocity field		✓	
Investigated the swirl effect on atomization			✓
Investigated the attenuating film thickness effect on film rupture			✓
Investigated droplet breakup in the near field			✓

This current work is an addendum to the previous work done in pressure-swirl atomization by Saha et al. (2012) and Lee et al. (2013). The significance of this work is that further influence of the swirling conical film and the breakup process of both the liquid film and droplets were examined. In particular, the swirl behavior, attenuating film thickness effect on film rupture were all investigated in order to add further insight into cascade atomization of pressure swirl atomizers. Table 1.2 catalogs both the previous work and the current work.

1.5 Outline Of This Thesis

In this thesis, cascade atomization phenomena is studied for pressure-swirl atomization. The novelty of this is work is in connecting liquid sheet dynamics dynamics and droplet dynamics with cascade atomization phenomena. This work also brings further insight into the swirling behavior and effect on film formation and breakup, which has never been shown before.

The experimental studies were conducted on a setup consisting of an autoclave and downward spray nozzle configuration in an open environment. The open environment allowed for the use of two different optical diagnostic systems, ultra-speed imaging and Phase Doppler Particle Anemometry (PDPA). Chapter 2 details the experimental setup used along with both diagnostic systems used. The ultra-speed imaging allowed for examinaton of the swirling liquid film and the fluctuations which occur on the interface of the film. The PDPA allowed for examination of droplet size and velocity profile and distribution and local points within both the near field and far field.

This work reports the correlation between linear 2-D analysis with the experimental observations of the swirling and undulating liquid film. In Chapter 3, theoretical analysis and experimental observations of the attenuating film thickness influence on the dynamics of the film have been delineated. Additionally, the influence of temporal instability on film rupture have been determined and classified.

Finally, Chapter 4 further explores the concept of cascade atomization in pressure-swirl atomization by examining the droplet dynamics. Moreover, a new theoretical model and criteria were developed to corroborate the influence of cascade atomization. The breakup and coalescence characteristics were examined for droplets in the near field and the far field.

CHAPTER 2: INSTRUMENTATION AND EXPERIMENTAL SETUP

2.1 Global Setup

The cascade phenomena was examined using three different simplex nozzles as the pressure-swirl atomizers. Table 2.1 displays the properties for each nozzle. Flow number, FN, represents the effective area which the fluid or spray covers. In other words, as flow number increases, the area exposed to the emanating spray increases.

Table 2.1: Properties for all three Nozzles used.

$FN(lb_m/hr/\sqrt{psi})$	Orifice Diameter(mm)
0.4	0.3
1.7	0.5
8	0.97

When fluid enters the nozzle, the flow is directed into a tangential port and into a swirl chamber. Once inside the swirl chamber, the fluid swirls around a circumferential diameter at a pitch angle. Once the swirling fluid reaches the orifice exit, the fluid emanates as a swirling liquid film. The internal geometry can be seen from figure 2.1.

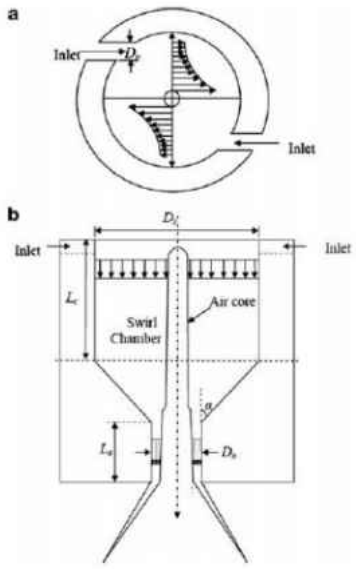

Figure 2.1: Geometry of the Swirl Chamber

However, in order for the swirling liquid film to radially expand, the inertia of the fluid must be very large. Therefore an autoclave was used as shown in figure 2.2. Liquid is poured into the autoclave and pressured with nitrogen gas. Once the desired autoclave pressure is reached, the fluid is passed through piping which ultimately leads to the nozzle. The operating autoclave pressures were from 3 bar to 32 bar.

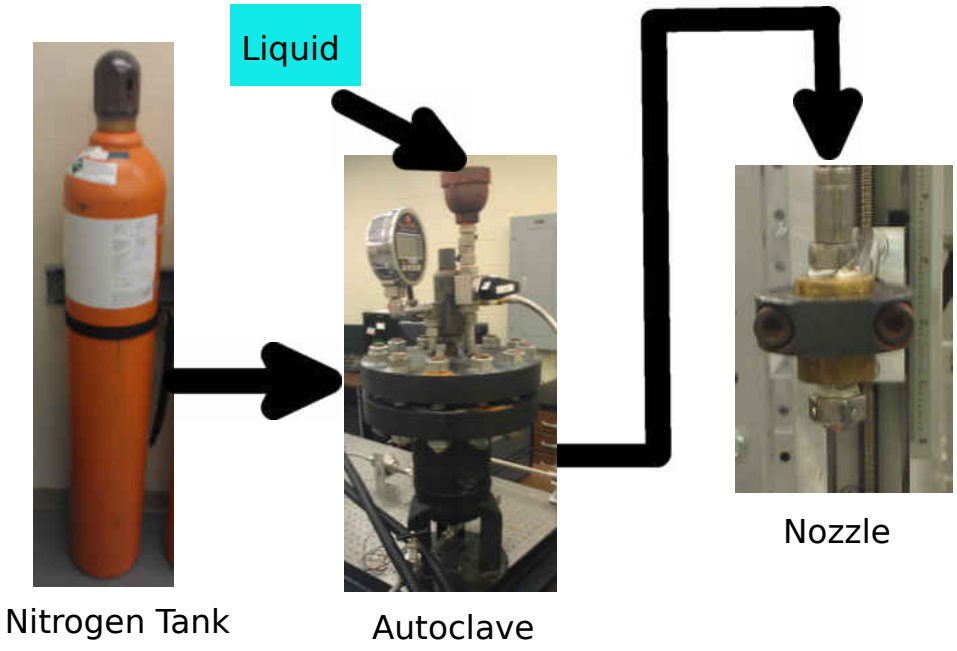

Figure 2.2: Liquid delivery system for the pressure-swirl atomizer.

Certain parameters can be calculated with the global setup alone. $U_{scale} = \sqrt{\frac{2\Delta P}{\rho_l}}$ is the theoretical velocity of the emanating liquid film(Kohnen et al. 2010). ΔP is the difference between the autoclave pressure and the ambient pressure and ρ_l is the density of the liquid. With this the Reynolds number can be calculated as $Re = \frac{\rho_l D_{orifice} U_{scale}}{\mu_l}$ where $D_{orifice}$ is the orifice diameter (can be found from Table 2.1) and μ_l is the dynamic viscosity of the liquid. Additionally, the Weber number for the liquid sheet can be calculated as $We_s = \frac{\rho_c h_0 U_{scale}^2}{\sigma}$ where ρ_c is the density of the ambient air, σ is the surface tension of the liquid, and h_0 is the film thickness of the liquid sheet near the orifice of the nozzle. The theoretical value for h_0 can be calculated as shown below in equation (Rizk and Lefebvre, 1985).

$$\dot{m} = FN\sqrt{\Delta P \rho_l} \tag{2.1}$$

$$h_0 = 3.66\left(\frac{\dot{m} D_{orifice}\mu_l}{\Delta P \rho_l}\right)^{1/4} \tag{2.2}$$

2.2 Ultra-Speed Imaging Setup

A Phantom V.12 camera was used to capture images of the swirling liquid film. The operating parameters for the camera are shown below in table 2.2. The camera's aperture was perpendicularly aligned with the axial direction of the swirling liquid film. An LED light source is aligned perpendicular with the axial direction of the swirling liquid film, but also in direct contact with the camera's aperture.

Table 2.2: Camera Settings

Frame Rate(fps)	Exposure Time(μs)	Resolution($pixel \times pixel$)
28000	10	512×256
130000	80	128×256

2.3 PDPA Setup

PDPA diagnostic system was used in order to analyze the droplet size and velocity distribution at local positions within the spray. A 632nm He-Ne laser is passed through a Bragg Cell which causes the laser to split into two beams with an optical frequency shift , $f_0 = 40MHz$. The two beams then intersect with beam separation of $50mm \pm 0.5mm$ and at a focal length of $310mm \pm 0.5mm$.

This creates a measuring volume where droplets pass through. In addition, the nozzle is attached to a traverse which allows for different locations of the spray to be measured. Figure 2.3 displays the configuration.

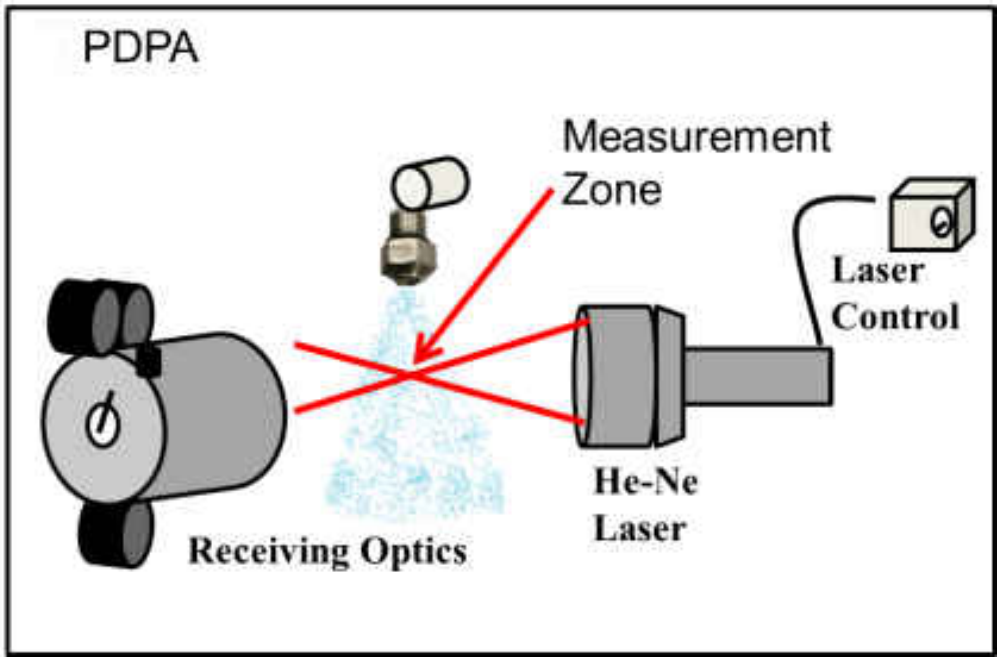

Figure 2.3: Liquid delivery system for the pressure-swirl atomizer.

Both the transmitting optics(laser) and the receiving optics are aligned in a forward scattering configuration with a scattering angle of 70^o. This configuration allows for first order refraction of scattered light to be received inside the aperture of the receiving optics. Three photodetectors are positioned at three different azimuthal angles $\alpha_{\Psi i}$ inside the receiving optics, where i represents the ith detector. Scattered light enters the aperture of a photodetector with a different scattering angle $\alpha_{\phi i}$. This causes a phase difference Φ_{ij} to occur.

$$n_{rel} = \frac{n_2}{n_1} \tag{2.3}$$

$$f_{i\pm} = 1 \pm \sin .5\alpha_\nu \sin \alpha_{\phi i} \sin \alpha_{\Psi i} + \cos .5\alpha_\nu \cos \alpha_{\phi i} \tag{2.4}$$

$$\alpha_{\beta i} = 2\left(\sqrt{1 + n_{rel}^2 - 2^{1/2} n_{rel} f_{i+}^{1/2}} - \sqrt{1 + n_{rel}^2 - 2^{1/2} n_{rel} f_{i-}^{1/2}}\right) \tag{2.5}$$

$$D = \frac{\Phi_{ij} \lambda_{pdpa}}{\Delta\alpha_{\beta ij} \pi n_1} \tag{2.6}$$

Because the first order refracted light is the dominant scattering mode, there exists a linear relationship between Φ_{ij} and the droplet diameter, D. This can be seen in equation 2.6 where λ_{pdpa} is the laser's wavelength(632 nm), n_1 is the index of refraction of air(1), n_2 is the index of refraction of the water droplet (1.334), and α_ν is the angle of the beam separation (Durst and Zaré, 1976).

$$C_{Rij} = A_{ij}(\tau) \cos\left(\omega_0 t + \Phi_{ij}\right) \tag{2.7}$$

$$C_{Iij} = A_{ij}(\tau) \sin\left(\omega_0 t + \Phi_{ij}\right) \tag{2.8}$$

$$\Phi_{ij} = \arctan \frac{C_{Iij}(0)}{C_{Rij}(0)} \tag{2.9}$$

Phase difference can be calculated using complex cross covariance functions of the signal difference detected between two photodetectors. This is shown in equation 2.9 where C_{Iij} is the imaginary component of the covariance function of the signal, C_{Rij} is the real component of the covariance function of the signal, A_{ij} is the envelope function of the signal, and ω_0 is the Doppler angular frequency (Lading and Anderson, 1989).

2.4 Uncertainty Analysis

As previously shown the size calculation of the droplets is based on both geometrical parameters and the signal processing of the scattered light. The maximum uncertainty from geometrical measurements such as the focal length and angle of beam separation is 1%. Additional, the system is calibrated such that only droplets emitting a signal with a signal to noise ratio of atleast 7 dB are validated and accepted. This equates to a signal to noise ratio of at least 5.01, or a maximum random error of 16% from the noise. However, since the scattered light gives information about the curvature of the droplets, the spherical deviation can be calculated between two photodetectors. Therefore, the maximum random error, from noise, can be further reduced by restricting the validation of droplets which have a maximum spherical deviation of 5%. This leads to a maximum phase error of 2%. Ultimately, the droplet diameter and velocity have an uncertainty of 4% and 2% respectively.

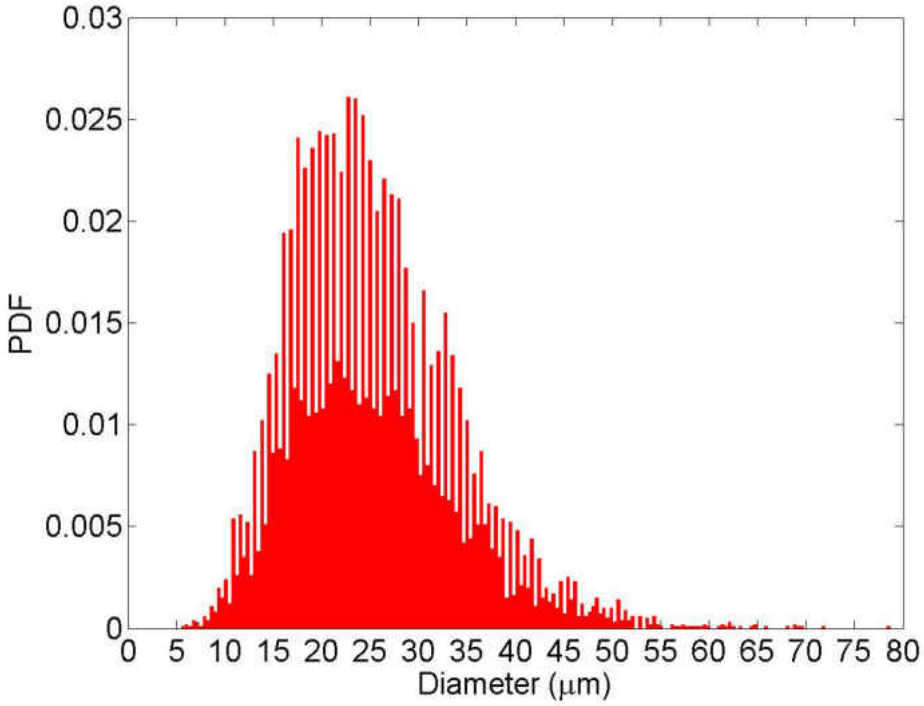

Figure 2.4: Droplet distribution for $FN = .4$ at $Re \approx 21000$.

In addition to error propagation, the polydispersed spray has an associated droplet size distribution at a given local point. It was observed that there was no significant change to the mean of the droplet size distribution after 10,000 samples. Figure 2.4 displays the typical distribution profile at a given location within the spray. Also, table 2.3 contains statistical information on the droplet size distribution at a location near-field and far-field along the axis of the spray.

Table 2.3: Mean and standard deviation of the droplet size distribution in the near-field and far-field.

FN	$D_{avg}(\mu m)$ near-field	$D_{S.Dev}(\mu m)$ near-field	$D_{avg}(\mu m)$ far-field	$D_{S.Dev}(\mu m)$ far-field
.4	25.4	$\pm$ 8.99	12.01	$\pm$ 5.36
1.7	41.3	$\pm$ 15.7	20.6	$\pm$ 8.79
8	41.2	$\pm$ 15.4	44.0	$\pm$ 13.8

CHAPTER 3: SHEET DYNAMICS

3.1 Liquid Film Morphology and Swirl Properties

Pressure Swirl atomizers are unique in that the film formation is dependent upon the centrifugal force of the swirling film. This dependency on the centrifugal force allows the film to undergo transition through different fluid flow states with different morphology. In other words, the centrifugal force changes the nature of the film formation and atomization process. This is clearly seen when examining the transient evolution of a liquid film, where the centrifugal force rapidly grows as the inertia of the liquid film reaches steady state.

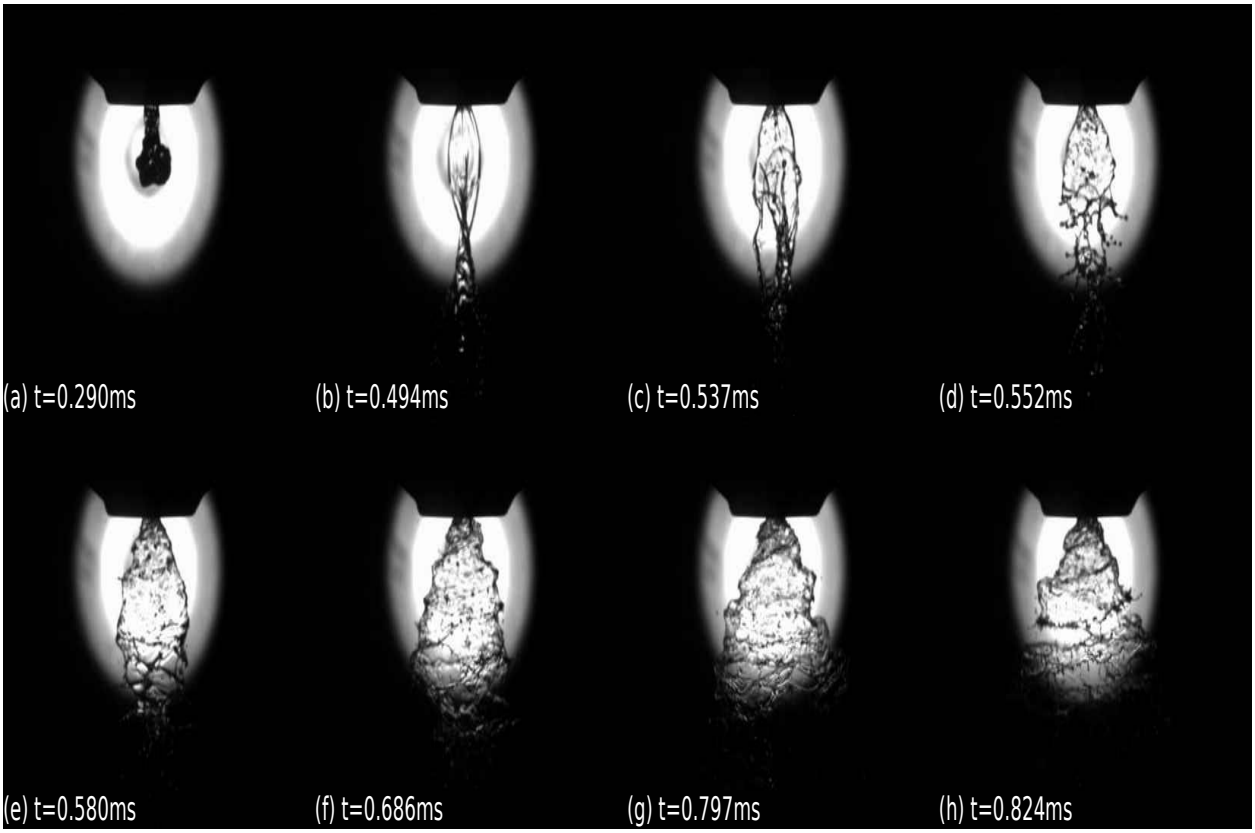

Figure 3.1: The transient evolution of a hollow cone spray at $FN = 8$ $Re \approx 21000$. All images were taken at a frame rate of 28,000 fps.

(a) Denser fluid accelerates and penetrates the ambient air in the form of a swirling jet. The mushroom-shaped head is caused by the Rayleigh Taylor instability generated by the acceleration of the film.

(b) Film begins to swirl but collapses due to pressure difference caused by surface tension. This state is often called the Onion stage.

(c) Liquid film radially expands more and begins to generate surface waves.

(d) Fluid agglomerates to form branches of stretched and recessed ligaments at the edge of the film.

(e) Liquid film is swirl stabilized with fluid agglomeration still occurring at the edge. This state is often called the Tulip stage.

(f) Waves become more prominent at the periphery of the liquid film.

(g)Liquid film radial expands and fluid is no longer agglomerating at the edge of the film.

(h)Liquid film has fully expanded and the film ruptures by wave disintegration.

Specifically, figure 3.1 demonstrates transition in film formation by display the transient evolution of a fully developed conical film. From figure 3.1(a) and figure 3.1(b), it is observed that the film begins as a swirling jet, and then expands into an annular jet which collapses due to a weak centrifugal force, which is unable to impede the pressure force. Both of these states are governed by Rayleigh Plateau instability, where the capillary motion causes the pinching of the neck,which ultimately leads to the formation of droplets. From figure 3.1(c) and figure 3.1(d), it is observed that the increase in centrifugal force causes the liquid film to expand radially. This radial expansion not only impedes film collapse, but also causes the film thickness to thin or attenuate. Moreover, figure 3.1(d) displays that surface waves have generated on thinner annular film with protruding ligaments at the edge of the sheet. The surface waves generated travel with a group velocity faster than film velocity. This causes the fluid to agglomerate at the edge of the film, thus forming protruding ligaments. Ultimately, the ligaments breakup due to capillary instability. From figures 3.1(e)-(g), it is observed that fluid agglomeration becomes smaller in magnitude as the film velocity is approaching steady state and the Kelvin-Helmholtz waves start to grow on the film periphery. The atomization in these states are considered rim disintegration, where the fluid still agglomerates, but breakup is assisted by the emerging growth of Kelvin-Helmholtz waves. Finally, from figure 3.1(h) the liquid film has reached steady state with a conical structure and the atomization process is governed by wave disintegration. Thus, the transient evolution encapsulates how not only how the film formation changes, but also how the atomization process changes.

In addition to the transient evolution, the same morphological transformations can be seen in steady state for an array of Reynolds Numbers and Weber Numbers. Given that the desired fluid flow state is in the conical state, it is of interest to investigate when the film transitions to conical flow. In order to investigate this transition, the swirl intensity was calculated and compared to the necessary swirl needed to stabilize a swirling annular sheet.

The calculation of swirl intensity given in Equation 3.1 cannot be determined with initial values

or control parameters alone. However, Alekseenko et. al. (1999) demonstrates, near the exit of the swirl chamber, Equation 3.1 can be approximated as Equation 3.2. Equation 3.2 is dependent entirely on geometrical parameters of the swirl chamber where $D_{chamber}$ represents the swirl chamber diameter, d_{core} represents the circumferential diameter upon which the injected fluid swirls around, and A_p represents total area of all the inlet ports.

$$S = \frac{\int_{A_p} \rho_d w u r \, \mathrm{d}A_p}{\frac{D_s}{2} \int_{A_p} P + \rho_d u^2 \, \mathrm{d}A_p}. \tag{3.1}$$

$$S \approx \frac{\pi D_{chamber} d_{core}}{4A_p} \tag{3.2}$$

Additionally, d_{core} can be represented by the air core diameter, at the orifice exit. Moreover, d_{core} can be substituted as shown below.

$$\begin{aligned} d_{core} &= D_{orifice} - 2h_0 \\ S &\approx \frac{\pi D_{chamber}(D_{orifice} - 2h_0)}{4A_p} \\ S &\approx \frac{\pi D_{chamber} D_{orifice}}{4A_p}\left(1 - \frac{2h_0}{D_{orifice}}\right) \end{aligned} \tag{3.3}$$

Thus, Equation 3.3 represents the inertial swirl intensity generated at the orifice exit of a given nozzle. Note that if h_0 is assumed to be zero, Equation 3.3 is identical to the inner Swirl parameter of a a coaxial swirl atomizer, derived by Sivakumar,Raghunandan (1998). The product $\frac{A_p}{D_{chamber} D_{orifice}}$ was calculated as $\sqrt{\frac{\pi(1-X)^3}{32X^2}}$, where $X = \frac{(D_{orifice}-2h_0)^2}{D^2_{orifice}}$. Both of these relationships are given by Suyari and Lefebvre(1998).

$$w_0^* = \sqrt{\frac{2}{We_{swirl}}} + \mathcal{O}\left(\frac{1}{R^3}\right) \tag{3.4}$$

$$S \approx \frac{w}{u} \tag{3.5}$$

$$w_0^* = \frac{w_0}{u_0}$$

$$S_{stable} \approx \sqrt{\frac{2}{We_{swirl}}} \tag{3.6}$$

Mehring and Sirignano (2001) demonstrated that for a swirling annular sheet, if centrifugal force is in excess, the swirl would destabilize and become conical. Equation 3.4 represents the non dimensional azimuthal velocity required to maintain a swirl stabilized state near the orifice, where $We_{swirl} \approx \frac{\rho_d U_{scale}^2 h_0}{\sigma}$. Given that Swirl intensity can also be approximated as equation 3.5, where w is the azimuthal velocity and u is the axial velocity, equation 3.6 represents the swirl intensity necessary to maintain swirl stabilized film. Henceforth, any values calculated using equation 3.6 will be referred to as stable swirl intensity.

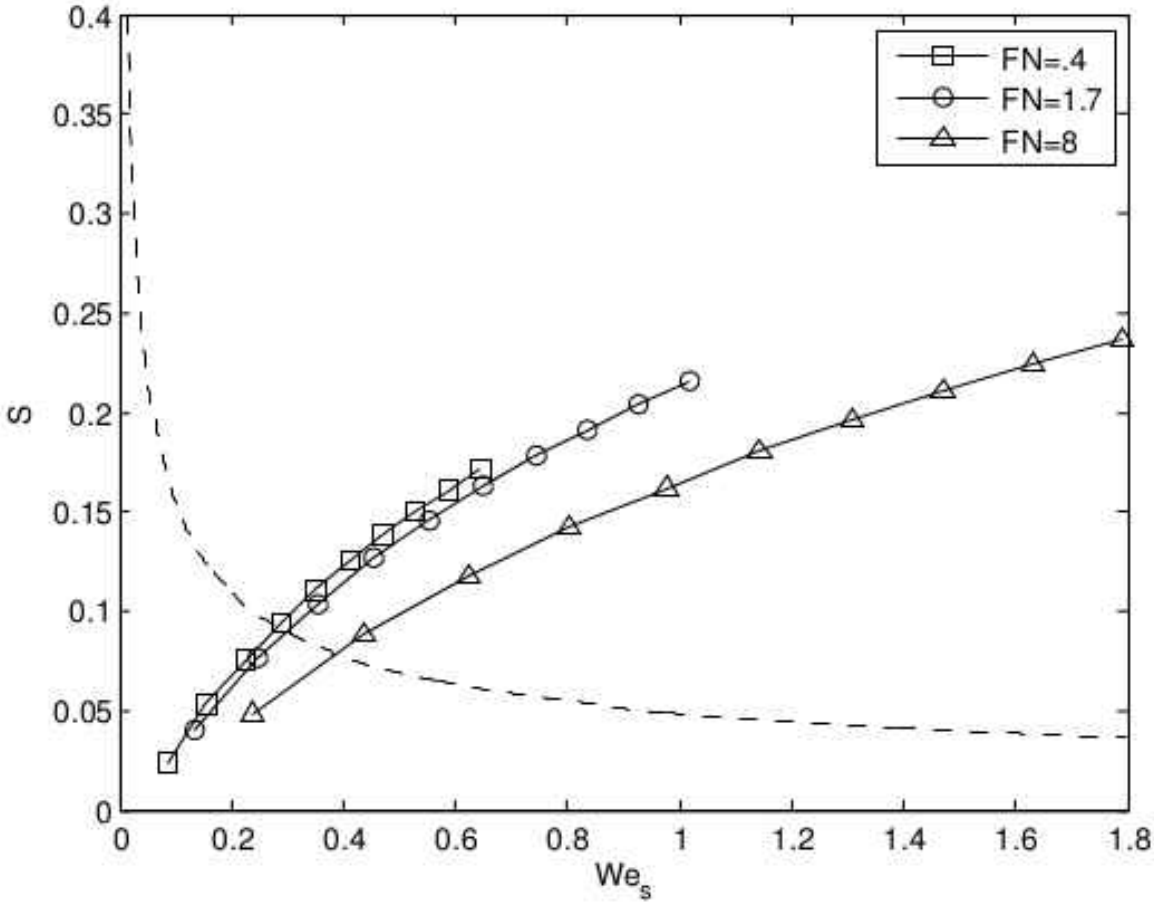

Figure 3.2: The Swirl Intensity for all three flow numbers. Solid line indicates the inertial Swirl number near the orifice of the nozzle. All three solid lines were calculated using equation 3.3, each line is calculated using a different flow number. Dashed line represents the Swirl Intensity needed to maintain Swirl Stabilized film, near the orifice of the nozzle. The dashed line was calculated using equation 3.6. Note $We_s = QWe_{swirl}$.

Figure 3.2 compares the inertial swirl intensity (near the orifice) of all three with the stable swirl intensity. Figure 3.2 demonstrates that inertial swirl intensity, for all three nozzles, increases beyond the stable swirl intensity approximately 0.5. It is also observed that the inertial swirl intensity is monotonically increasing, while the stable swirl intensity is monotonically decreasing. Both of these observations indicate swirl intensity for all three nozzles becomes in excess at a

relatively low We_s. Therefore, it can be concluded that the liquid film generated by all three nozzles will maintain a thin conical sheet formation. It is also seen that FN=8 requires a larger We_s than FN=1.7 and FN=.4 to become in excess of swirl.

3.2 Radial fluctuations

Figure 3.3: Image processing sequence for quantifying the outer interface of the conical film. (a) The original image of a of a film formed from a nozzle with $FN = 8$. (b) Background is subtracted and the image is threshold and converted to binary. The threshold image is such that the film's pixel value is 0, while the rest of the image has a pixel value of 1. (c) The original image with the outer interface traced and the axis located. The solid red line represents radial location of the film for every z location. The dashed red line represents the axis of the film.

In order to further investigate the film behavior, the curvature of the outer interface was measured in both space and time. This was accomplished by the use of a Phantom V.12 camera operated at a frame rate of 130,000 fps. Thousand images were collected for a given Reynolds number for all three Flow Numbers. Figure 3.3 displays how the images were processed such that the curvature could be measured. Essentially a threshold was applied such that only the liquid sheet remained within the image. This allowed for easy detection of the outer interface and collection of the radial position data with respect to time and the axial location.

$$r_{avg} = \frac{1}{T}\int_0^T r(t)\,\mathrm{d}t$$

$$r_{avg} = \frac{1}{n\Delta T}\sum_{i=1}^{n} r_i \Delta T$$

$$r_{avg} = \frac{1}{n}\sum_{i=1}^{n} r_i \tag{3.7}$$

$$r_i' = r_i - r_{avg}$$

$$r'(t) = r(t) - r_{avg} \tag{3.8}$$

$$r_{rms}' = \sqrt{\frac{1}{n}\sum_{i=1}^{n}(r_i')^2} \tag{3.9}$$

Moreover, time series data was collected at all axial location. Since the data points were taken at discrete time steps, time averaged value of r can be represented by the ensemble average as shown in equation 3.7. With the ensemble average, radial fluctuations can be calculated by using equation 3.8. Additionally, the root mean square of the radial fluctuations was calculated using equation 3.9.

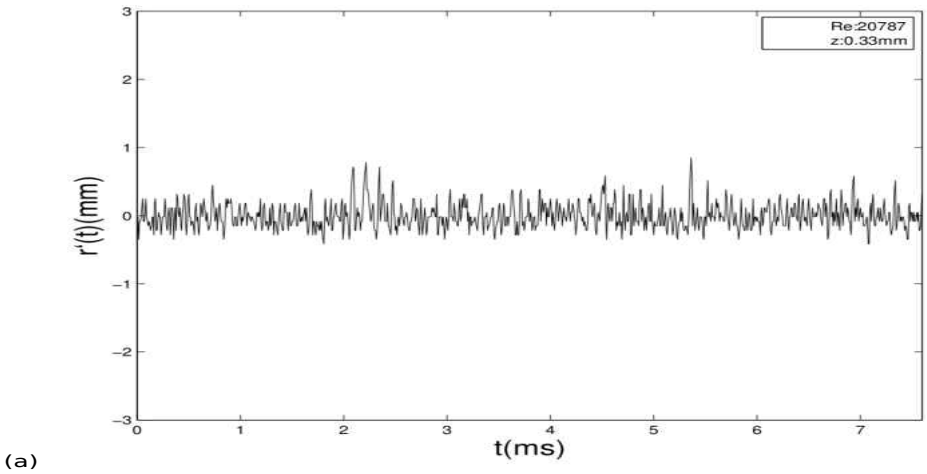

(a)

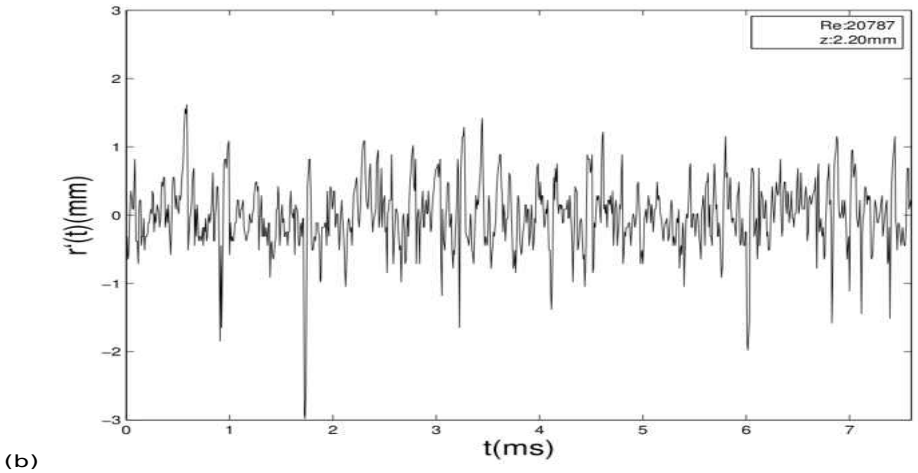

(b)

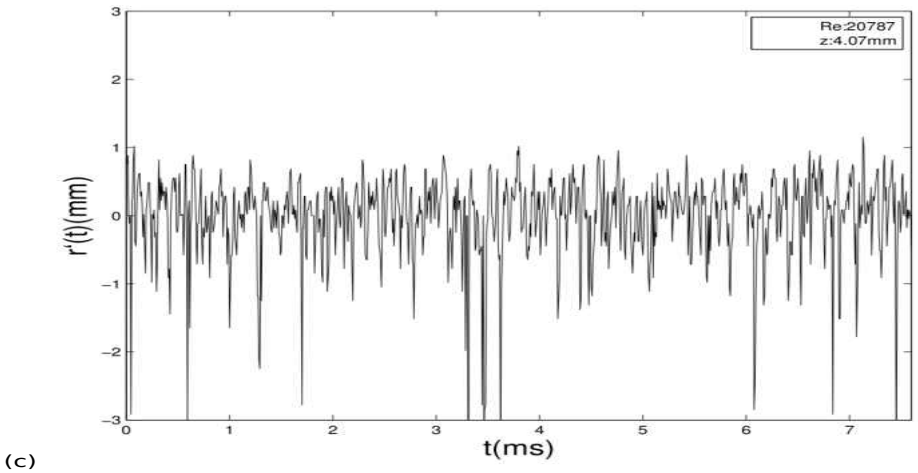

(c)

Figure 3.4: Represents the $r'(t)$ at three different axial locations. (a) Near orifice (b) Away from the orifice but prior to rupture (c) Rupture regime

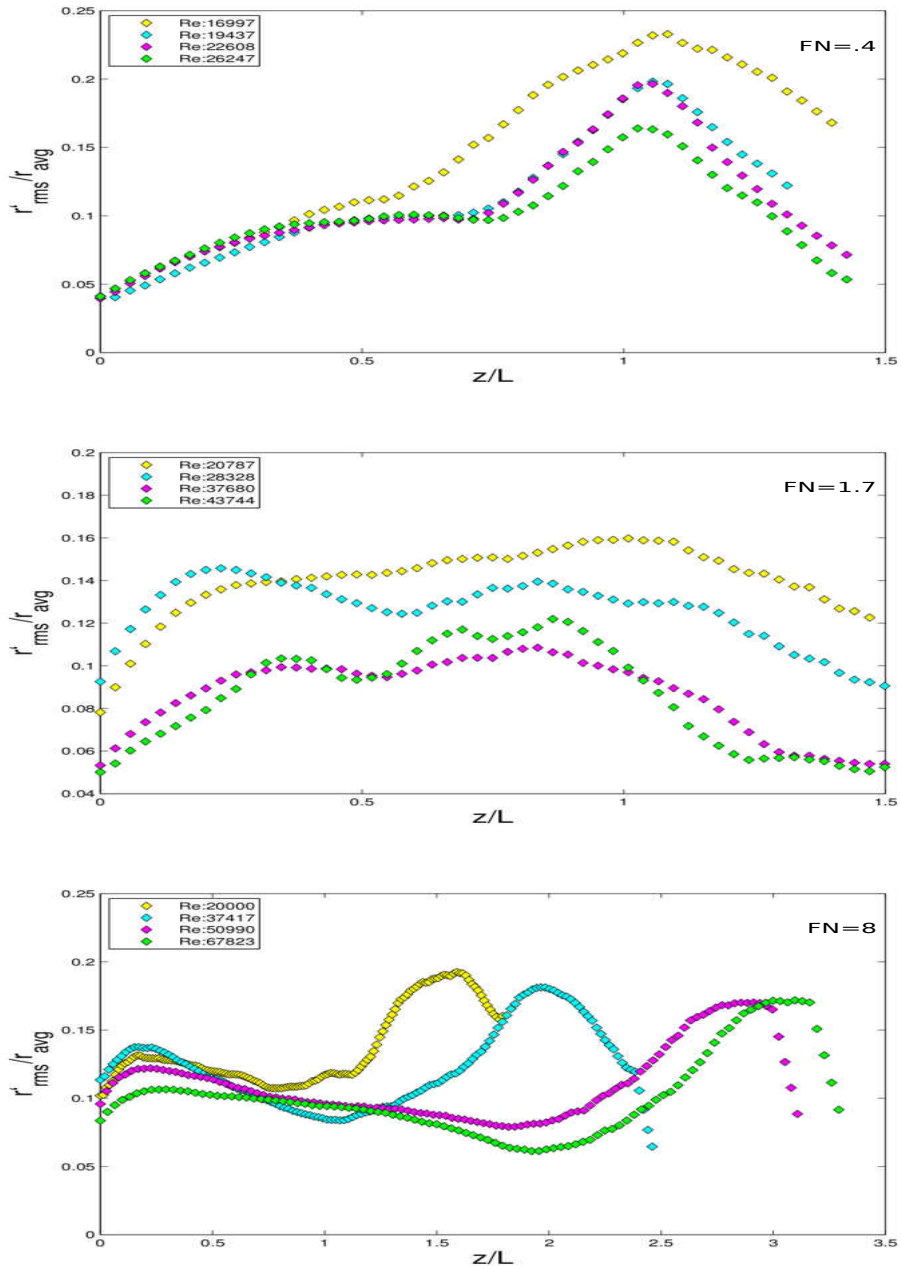

Figure 3.5: Represents the radial fluctuation intensity, r'_{rms}/r_{avg}, for varying Reynolds number. Note that the axial position is non dimensionalized by the theoretical breakup length L, where $L = \frac{U_{scale}}{\Omega_s} \ln \frac{\eta_b}{\eta_0}$, given by Senecal et. al. (1999). $ln\frac{\eta_b}{\eta_0} \approx 12$ which is the correlation given by Dombrowski and Hooper(1962). (a) for FN=.4 (b) for FN=1.7 (c) for FN=8.

From figure 3.4 it is observed that the fluctuations become higher further downstream. This observation indicates that the outer interface propagates (in time) with larger amplitude , the closer the dispersive waves travel towards the breakup regime. It should also be noted from figure 3.4 (c) that the large fluctuations are occurring mainly in the negative direction. This is due to the occurrence of cascading breakup where the film ruptures and then subsequently torn liquid filaments undergo further breakup. Essentially there is very little positive fluctuation because the torn filaments travel along the periphery of the cone.

Figure 3.5 (a)-(c) shows that the radial fluctuation intensity reaches a peak, for all Flow Numbers, and at each specified Reynolds Number. This peak represents the maximum fluctuations which occur due to the liquid film breaking up. Additionally, for a given flow number, with an increase in Reynolds number, the attenuation of the film thickness occurs much quicker or the gradient with respect to the axial location becomes steeper. Therefore, the rupture of the film can occur with a smaller unstable amplitude or smaller fluctuation intensity, because the film thickness is smaller at all axial locations. This is also observed from 3.5 (a) where the radial fluctuation intensity decreases at the point of rupture as Reynolds Number increases.

Similarly, the same decrease in radial fluctuation intensity can be observed for 3.5 (b). In contrast, from figure 3.5 (b), the peak described from 3.5 (a) appears to diminish. However, as Reynolds number increases, it is observed that the peak begins to bifurcate. The breakup or rupture of the film is indicated by the second peak.

Lastly, from figure 3.5 (c), the bifurcation of the peaks becomes distinct for FN=8. Additionally, the peaks differ in magnitude, such that the first peak is smaller than the second peak. In comparison with FN=1.7, the second peak indicates the breakup of the film. It should be noted that the length scale L is a linear length scale, therefore any nonlinear contributions to breakup would not be indicated by the use of L. To elucidate any ambiguity contributed from nonlinear effects,

both inspection and comparison of the photographs with figure 3.5 (c). From this inspection, it is observed that second peak is correlated with the location of the film breakup which is comparable to the case of FN=1.7. Conversely, it is observed that beyond $Re \approx 20000$, the linear length scale L is no longer an accurate predictor of the breakup for FN=8. Therefore, it can not be deduced that as Reynolds number increases, film rupture occurs further downstream.

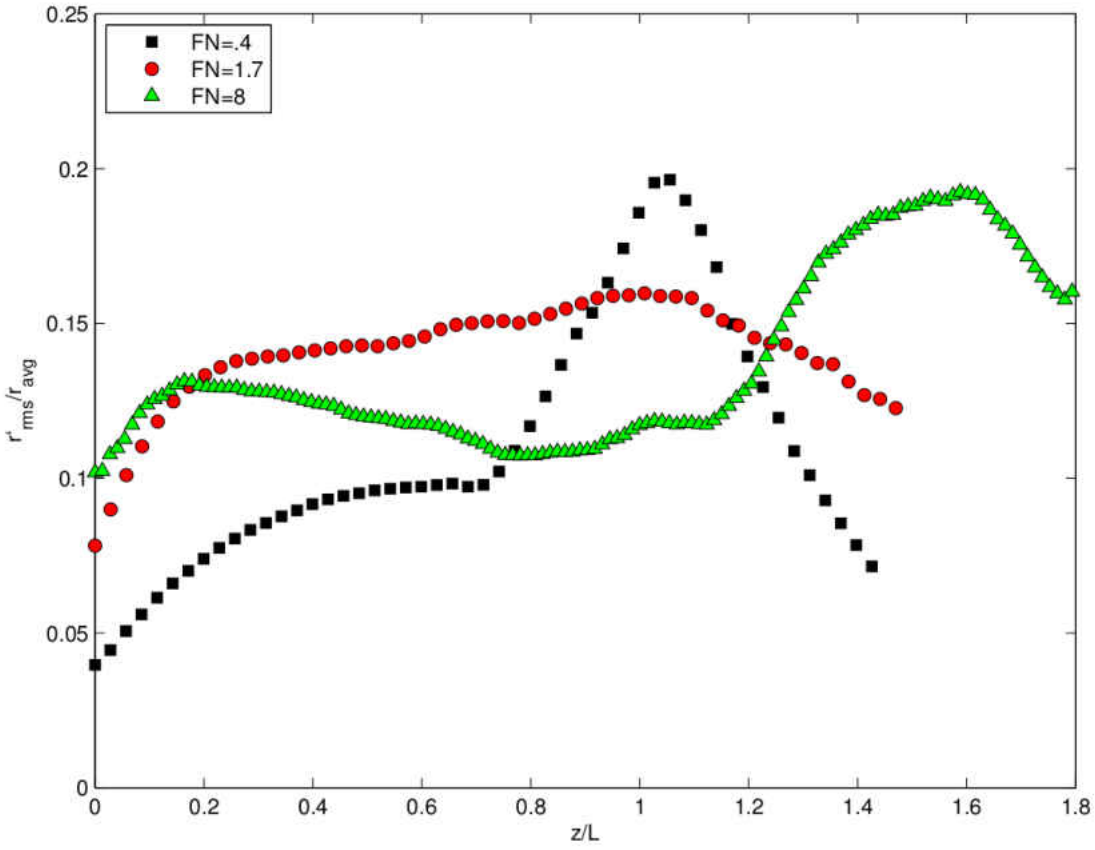

Figure 3.6: Comparison of the radial fluctuation strength for all three Flow numbers at $Re \approx 22000$.

From figure 3.6, it is demonstrated that a peak will bifurcate into two peaks which ultimately display growing oscillatory behavior, as flow number increases. Jazayeri and Li (2000), have

demonstrated similar behavior occurs in a thin plane liquid sheet exposed to nonlinear instability. Specifically, their findings have shown that the first (linear) harmonic of the sinuous did not lead to break, despite being unstable. Instead it was actually the higher harmonics which cause the rupture of a thin plane liquid sheet by introducing small varicose disturbances.

The key distinction between the work of Jazayeri and Li and the current work, is that Jazayeri and Li assumed a constant film thickness where this work accounts for the effect of the attenuating film thickness. This implication is profound because it demonstrates that for a small flow number, attenuation of the film thickness supersedes the long term behavior of nonlinear instability. Rangel and Sirignano (1991) supports this conjecture, where their findings demonstrated that nonlinear effects occur on slower varying time scale. However, it should be noted that the converse is true as well, where for larger flow number, the long term behavior of nonlinear instability contributes and is coupled with the attenuation of the film thickness to cause breakup of the film. This is possible because for larger flow numbers, the spatial average of the film thickness becomes larger, regardless of attenuation. Therefore, the film thickness will become thin at a longer time scale before breaking up.

3.3 Wavelength Characteristics

Squire(1953), Hagerty and Shea(1955), and Taylor(1959) were some of the first to demonstrate the existence of dispersive waves on the surface of thin-liquid moving sheets. Dispersive waves are unique in that each wave in a given wave packet, or wave train, travels at a phase speed which is dependant upon the wave number or angular frequency. Alternatively, the angular frequency is dependent upon the wave number. This coupled behavior between the angular frequency and wave number makes it quite difficult to experimentally analyse the temporal and spatial characteristics of the surface waves generated on thin-liquid moving sheets. Therefore, a clearer interpretation

would be to examine the asymptotic behavior of dispersive waves. In other words, examination of either very short wavelengths or very long wavelengths are feasible and easy to measure for comparison with theory.

Saha et. al.(2012) had shown accurate comparison of experimentally measured wavelengths near the rupture location with the asymptotic values for both the dominant long wavelength for inviscid temporally-unstable growth rate and dominant short wavelength for inviscid temporally-unstable growth rate. While Saha et. al.(2012) demonstrated the transition from long wavelength to short wavelength, they stated that the sample size was only as large as thirty images. Therefore, the scatter of their predicted mean(for short wavelength measurements) was large. It should also be noted that there are very few measurements within the short wavelength dominant regime(defined by Senecal et. al. 1999). Additionally, Mehring and Sirignano(1999) and Villermaux and Clanet(2002) have reported that short wavelengths can be on the order of molecular scale.

The measurement of maximum wavelengths undulating on the surface of a swirling liquid film is possible from Ultra-speed imaging. Given the difficulties arising from the length scale of short wavelengths, only comparison with long wavelength solutions are usually performed. In this work,a new long wavelength solution is derived to include the effect of film thickness which is attenuating and approaching zero.

As previously shown, the attenuation of the film thickness contributes to the breakup and/or rupture of the conical film. In order to investigate the contribution of the attenuation of film thickness as the film thickness approaches zero, an expression for the film thickness with respect to 'r' is needed.

Matsumoto and Takashima (1971) demonstrates that sheet velocity remains relatively constant up to the point of breakup. Thus, if we consider the attenuation of the undisturbed conical film, mass conservation can be used to find an expression for film thickness with respect to r.

$$\dot{m} = U_0 \rho_d \pi \left(r^2 - (r-h)^2 \right) \tag{3.10}$$

$$h(r) = \frac{2r - \sqrt{4r - \frac{4\dot{m}}{U_0 \rho_d \pi}}}{2}$$

$$h(r) = r - \sqrt{r - M} \tag{3.11}$$

As shown above, equation 3.11 represents the attenuation of film thickness as r increases, where $M = \frac{\dot{m}}{U_0 \rho_d \pi}$. While equation 3.11 is accurate, the interest of film thickness behavior is within the limit as h nears 0, or conversely the limit when r becomes very large. Thus to examine this limit, h is expanded in terms of $\delta_n \left(\frac{1}{r}\right)$ as shown below.

$$h(r) = r - r\sqrt{1 - \frac{M}{r^2}}$$

$$h(r) = r - r\left(1 - \frac{M}{r^2} - \frac{M^2}{8r^4} + \mathcal{O}\left(\frac{1}{r^6}\right)\right)$$

$$h(r) = \frac{M}{2r} + \frac{M^2}{8r^3} + \mathcal{O}\left(\frac{1}{r^5}\right) \tag{3.12}$$

$$h(r) \sim \frac{M}{2r} \tag{3.13}$$

Equation 3.12 represents the asymptotic expansion of h. Furthermore, since only h's behavior for very large r is of interest, the first term truncation becomes an accurate approximation, which is shown as equation 3.13. Also note that the $\frac{\mathrm{d}h}{\mathrm{d}r} = \mathcal{O}\left(\frac{1}{r^2}\right)$. Therefore the use of equation 3.13 will also include the attenuating behavior, since equation 3.13 is $\mathcal{O}\left(\frac{1}{r^3}\right)$ accurate.

$$\omega = \frac{U_0 k \tanh(kh/2)}{tanh(kh/2)+Q} \pm \frac{(\sigma k^3(\tanh(kh/2)+Q)/\rho_d - QU_0^2 k^2 \tanh(kh/2))^{\frac{1}{2}}}{\tanh(kh/2)+Q}$$

$$\omega = \frac{U_0 k}{1+Q/\tanh(kh/2)} \pm \frac{1}{1+Q/\tanh(kh/2)} \left(\frac{\sigma k^3}{\rho_d \tanh(kh/2)} + \frac{Qk^3\sigma}{\rho_d \tanh^2(kh/2)} - \frac{QU_0^2 k^2}{\tanh(kh/2)} \right)^{\frac{1}{2}}$$

$$\omega = \frac{U_0 k}{1+2Q/kh} \pm \frac{1}{1+2Q/kh} \left(\frac{2\sigma k^2}{U_0^2 \rho_d h} + \frac{2A\sigma k}{U_0^2 \rho h^2} - \frac{2Qk}{h} \right)^{\frac{1}{2}} \tag{3.14}$$

Given that small film thickness approximation is identical to the long wave approximation, Squire's result, as shown above, can be simplified to equation 3.14.

$$\tilde{\omega} = \frac{\omega\sqrt{M}}{U_0}, \tilde{r} = \frac{r}{\sqrt{M}}, \tilde{k} = k\sqrt{M}, We_l = \frac{\rho_d \sqrt{M} U_0^2}{\sigma}$$

$$\tilde{\omega} = \frac{\tilde{k}}{1+4Q\tilde{r}/\tilde{k}} \pm \frac{\sqrt{M}}{1+4Q\tilde{r}/\tilde{k}} \left(\frac{4\tilde{k}^2\tilde{r}}{We_l} + \frac{8Q\tilde{k}\tilde{r}^2}{We_l} - 4Q\tilde{k}\tilde{r} \right)^{\frac{1}{2}}$$

$$\tilde{\omega} = \frac{\tilde{k}}{1+4Q\tilde{r}/\tilde{k}} \left(1 \pm \left(\frac{4\tilde{r}}{We_l} \left(1 + \frac{2Q\tilde{r}^2}{\tilde{k}} \right) - \frac{4Q\tilde{r}}{\tilde{k}} \right)^{\frac{1}{2}} \right) \tag{3.15}$$

$$\tilde{\omega} = \tilde{\omega_r} + i\tilde{\omega_i}$$

$$\tilde{\omega_r} = \frac{\tilde{k}}{1+4Q\tilde{r}/k} \tag{3.16}$$

$$\tilde{\omega_i} = \frac{\sqrt{4Q\tilde{k}\tilde{r}}}{1+4Q\tilde{r}/\tilde{k}} \left(1 - \frac{4\tilde{r}}{We_l} \left(1 + \frac{\tilde{k}}{4Q\tilde{r}} \right) \right)^{\frac{1}{2}} \tag{3.17}$$

Using $\sqrt{M}$ as a length scale l, variables in equation 3.14 can be non-dimenionalized. After nondimensionalization, equation 3.13 can be substituted into equation 3.14 to produce equation 3.15. If equation 3.15 is decomposed into real part and imaginary, the results are equation 3.16 and 3.17, respectively.

$$\tilde{c}_g = \frac{\partial \tilde{\omega}_r}{\partial \tilde{k}}$$

$$\tilde{c}_g = \frac{1 + 8Q\tilde{r}/\tilde{k}}{(1 + 4Q\tilde{r}/\tilde{k})^2} \tag{3.18}$$

$$s(\tilde{k}, \tilde{x}) = \ln\left(\frac{\eta(\tilde{k}, \tilde{x})}{\eta(\tilde{k}, 0)}\right) = \int_0^t \omega_i \, \mathrm{d}t = \int_0^{\tilde{x}} \omega_i \frac{\mathrm{d}x}{c_g}$$

$$\mathrm{d}x = \frac{\mathrm{d}r}{\sin\alpha}$$

$$s(\tilde{k}, \tilde{r}) = \frac{1}{\sin\alpha} \int_0^{\tilde{r}} \frac{(4Q\tilde{k}r^{\frac{1}{2}}(1 + 4Qr/\tilde{k})}{(1 + 8Qr/\tilde{k}} \left(1 - \frac{4r}{We_l} - \frac{\tilde{k}}{QWe_l}\right)^{\frac{1}{2}} \mathrm{d}r \tag{3.19}$$

$$\tilde{r}_{max} = \frac{We_l}{4} - \frac{Q\tilde{k}}{4} \tag{3.20}$$

With ω_r the group velocity was calculated and is represented by equation 3.18. Using the group velocity, the integral within the amplification factor can be converted with respect to x, where x represents the cone slope direction. For an undisturbed conical film, x can be described in terms of both r and α, the half cone angle. Combining all these transformations, results in the amplification factor as described by equation 3.19. Equation 3.19 can not be examined analytically, however with the use of Leibniz rule the maximum $\tilde{r}_{max}$ can be found (equation 3.20).

$$\tilde{k}_{max} = \frac{We_{\sqrt{M}}Q + \sqrt{We^2_{\sqrt{M}}Q^2 - 4}}{2} \tag{3.21}$$

$$\frac{\lambda_{max}}{h_0} = \frac{\sqrt{M}}{h_0} \frac{4\pi}{We_{\sqrt{M}}Q + \sqrt{We^2_{\sqrt{M}}Q^2 - 4}} \tag{3.22}$$

With $\tilde{r}_{max}$ known, equation 3.20 can be substituted into equation 3.17 to find the dominant k

at which maximum growth rate occurs. Equation 3.22 represents the dominant wavelength. With $\tilde{k}_{max}$ known, the scaled theoretical wavelength can also be found and is represented by equation 3.22.

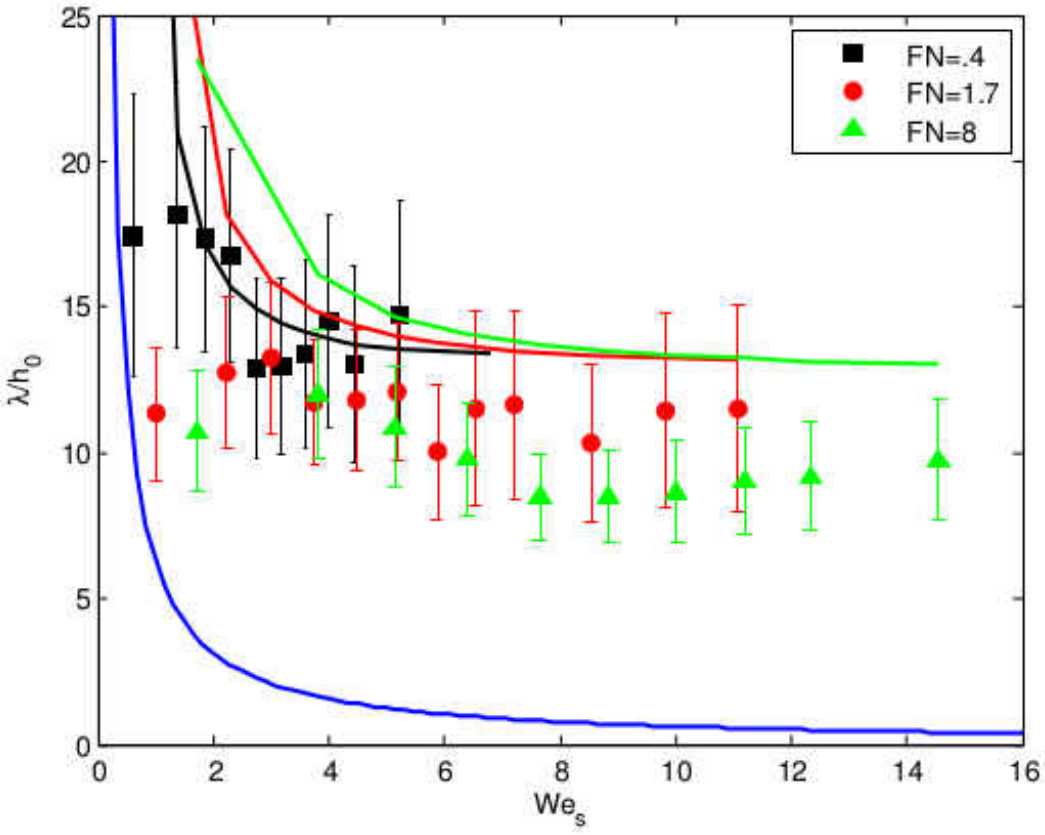

Figure 3.7: Maximum wavelengths measured for FN=.4, 1., 8. The error bars represent $\pm$ 1 standard deviation. The solid black,red,green line represents the theoretical dominant wavelength (for maximum growth rate) of the asymptotically small h or large R approximation (calculated using equation 3.22, for $FN = 4$ $FN = 1.7$ $FN = 8$ respectively. The solid blue line represents the dominant wavelength for long wave approximation ($\approx \frac{2\pi}{We_s}$).

From the photographs, the maximum wavelength along the periphery were measured. The mean and standard deviation were calculated using a sample size of 1000 images. This was done for each Weber Number. Along with equation 3.22, the dominant wavelength for long wave approximation

was also calculated and compared with the measured results. This comparison can be seen in figure 3.7.

From figure 3.7 it is observed that approximately around $We_s \approx 2-6$, equation 3.22 is similar to the measured wavelengths, for all three nozzles. Below $We_s \approx 2$, the measured wavelengths appear to match more closely with the long wave approximation. For both FN=.4 and FN=1.7, equation 3.22 is in good agreement. However from $We_s \approx 8$ and above, FN=8 deviates away from the small thickness assumption.

Another interesting observation, is that the small thickness approximation represents the upper bound, where the long wavelength and constant thickness approximation represents the lower bound. This indicates that temporally unstable Kelvin Helmholtz waves are able to grow larger on films which are attenuating, as opposed to films which are small but relatively constant.

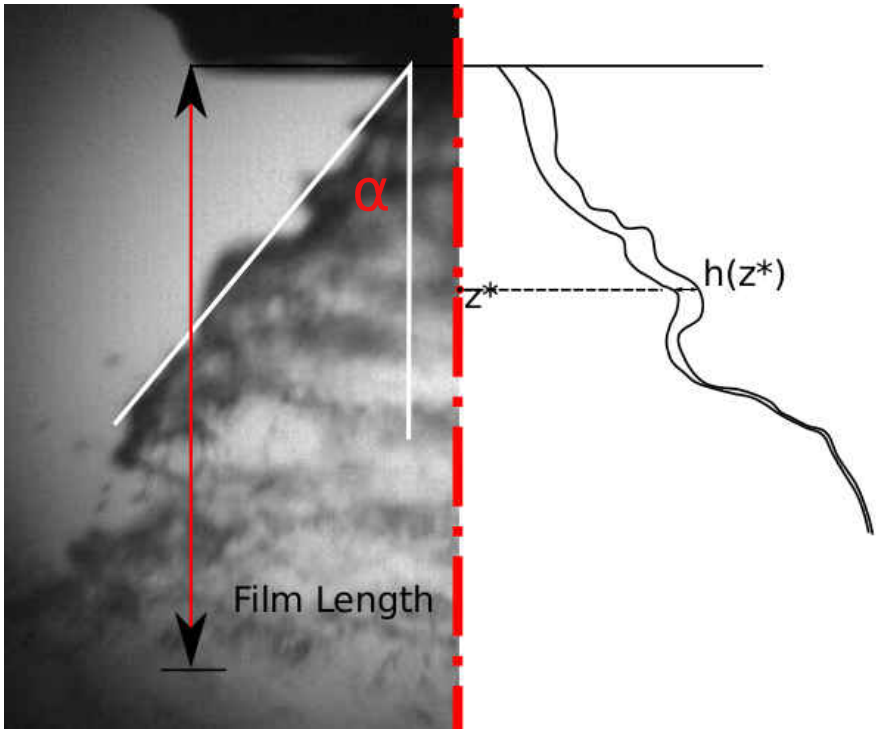

Figure 3.8: Image of a Conical Film. α represents the half angle of the cone. The film length is determined as the length at which the film breaks up or ruptures from the base of the nozzle. It should also be noted that the film thickness is defined as the difference between the inner and outer interface. For a sinuous mode of breakup, both interfaces deflect symmetrically.

From Ultra-speed images, the film length, cone angle can be determined. Figure 3.8 shows how both the film length and cone angle be measured. Additionally it can be seen how film thickness can be measured using the interface.

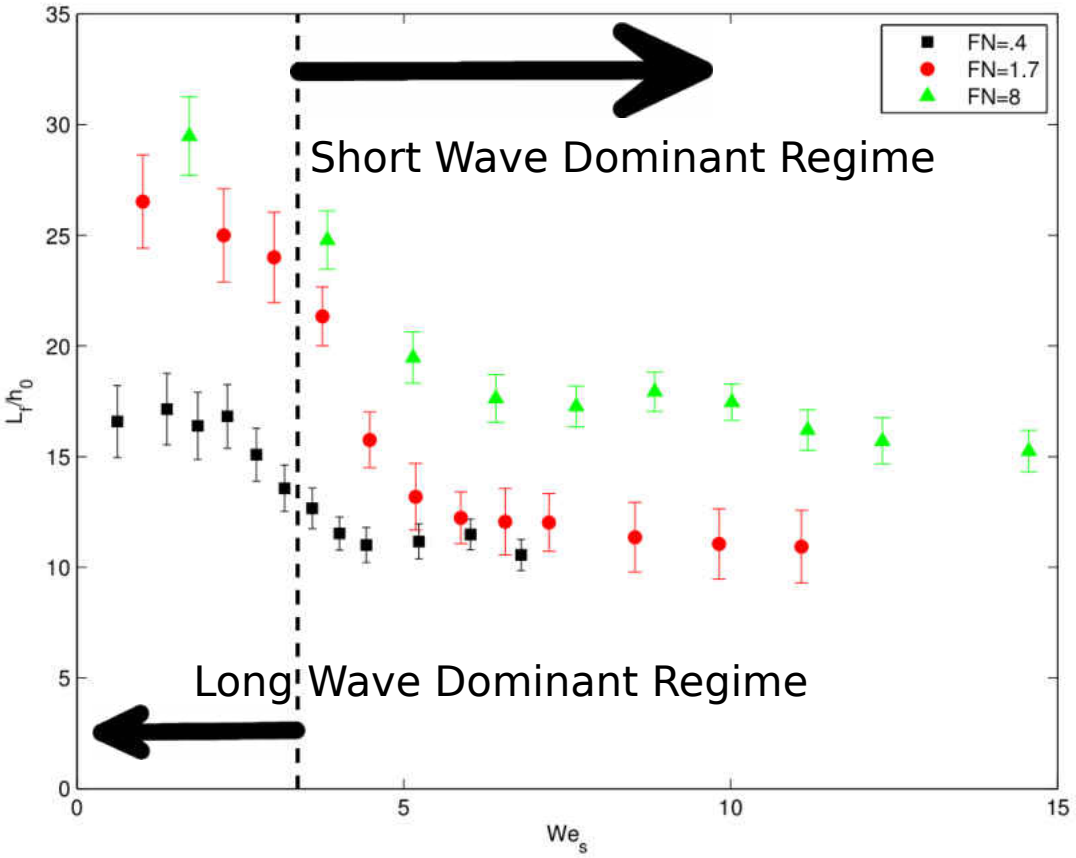

Figure 3.9: Film Length for all three nozzles ($FN = .4$ $FN = 1.7$ $FN = 8$) with respect to We_s. The dashed line indicates the critical line ($We_s \approx 27/8$ which delineates the long wave dominant regime and short wave dominant regime as determined by Senecal et al.(1999). It should be noted that Senecal et al.(1999) used half film thickness as the length scale. In this study, the length scale is the full film thickness,h_0, therefore the critical value which Senecal et al. (1999) discovered ($We_s \approx 27/16$) was multiplied by 2.

From the previous section, it was determined that short wavelengths scale can be as small as a molecule. However, this does not imply that short wavelengths do not effect the breakup behavior of a liquid film. Instead, after a critical value short wavelengths have a more dominant effect than long wavelengths. This can be observed from figure 3.9 where below $We_s \approx 27/8$, the film length decreases with a slight descent. However, beyond $We_s \approx 27/8$ the film length decreases with a

steeper slope before reaching a asymptotic value. This behavior is seen for all three flow numbers. This delineation is analogous the the breakup regime map developed by Reitz and Bracco (1992).

Reitz and Bracco(1992) discovered that for jet breakup, there exists a primary dominant Rayleigh Plateau instability regime, first wind induced regime, second wind induced regime, and finally full atomization regime. Moreover, depending on the Weber number, the breakup mode would transition through all aforementioned modes. In our current, study only two regimes were identified. However, from the previous section it was determined that for a swirling sheet at low We_s there is a possibility of sheet collapse or rim disintegration. Rim disintegration is a mode of breakup driven by capillary instability due to the meso-scale formation of ligaments. Additionally, Mehring and Sirignano(2000) determined that both varicose and sinuous mode of instability were coupled in a swirling annular sheet (not in excess swirl). Also, if $FN = 8$ is observed beyond We_s there seems to exist a region where the asymptotic behavior is relaxed and the film length begins to descend again. It is speculated that this region is the onset of shear instability where the boundary layer formed by the continuous phase begones to separate causing further instability coupling. To summarize, the long wavelength dominant regime includes breakup by both capillary instability and Kelvin Helmholtz instability, while the short wavelength dominant regime is mainly dominated by short Kelvin Helmholtz waves. Lastly, there exists a shear-induced breakup regime where viscous continuous phase now must be considered.

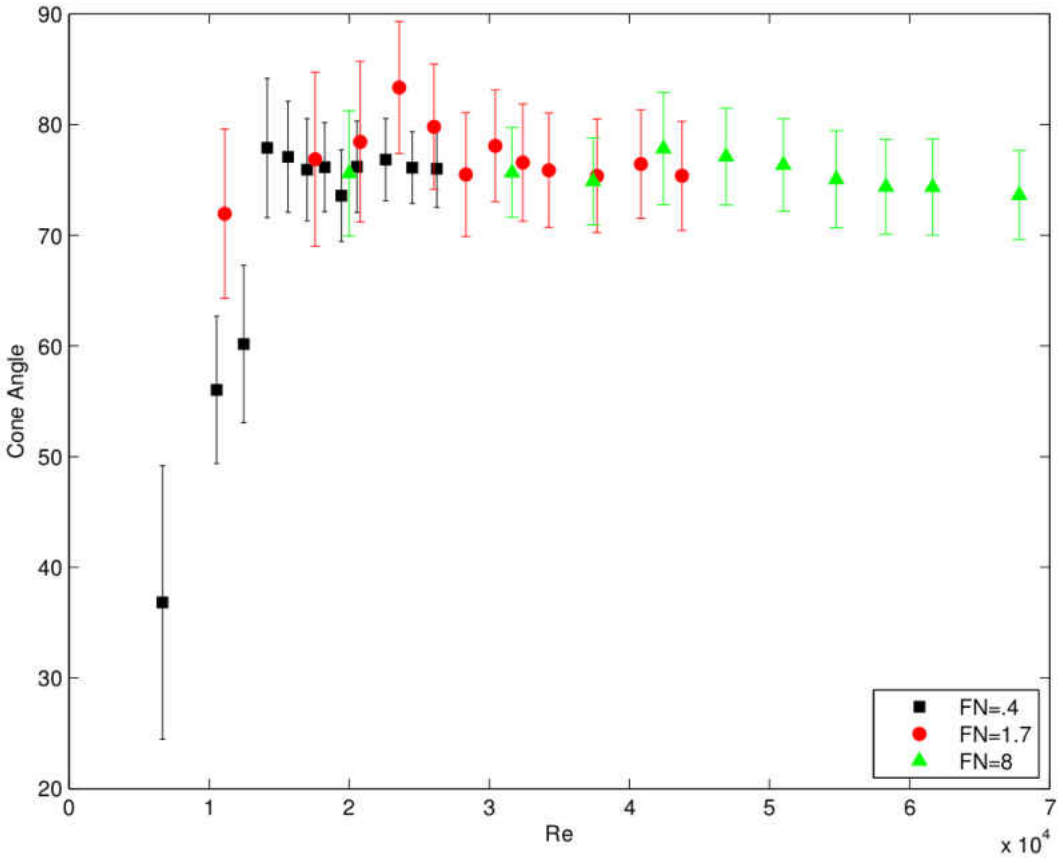

Figure 3.10: Cone angle for all three flow numbers with Respect to Reynolds Number.

In addition to the film length, the cone angle for all three nozzles was measured. From figure 3.10 it is observed that the cone angle reaches an asymptotic value near ≈ 80 for all three nozzles. It should also be noted that all three nozzles were manufactured by the same company and are part of the same series. To clarify, the cone angle ceiling observed, for all three nozzles is due to the internal geometry of the pressure swirl atomizers. Additionally, because of the viscosity there is momentum loss to the boundary layer within the swirl chamber. Therefore while swirl chamber pitch angles are often small, the liquid film will never expanded near the value of 180 degrees.

CHAPTER 4: DROPLET DYNAMICS

4.1 Diameter and Velocity Profile

To segue into droplet analysis, a semi-quantitative analysis was conducted to examine the transitional behavior from sheet breakup to droplet formation. Equation 4.1 was used to examine the growth rate of the unstable waves generated on the surface of the conical sheet. Senecal et al. (1999) derived equation 4.1 from his dispersion relationship for a 2-d viscous sheet moving in inviscid-ambient gas. Equation 4.1 was used for all three flow numbers (FN=.4, 1,7,and 8), for both $\sigma = 70mN/m, 48mN/m$ at a constant $Re \approx 21000$. Figure 4.1 represents the growth rate for all 6 cases.

$$\omega_{i_{visc}} = \frac{\sqrt{4\nu_s k^4 \tanh^2 kh - \left(\frac{\rho_c}{\rho_s}\right)^2 U^2 k^2 - \left(\tanh kh + \frac{\rho_c}{\rho_s}\right)\left(\frac{\sigma k^3}{\rho_s} - \frac{\rho_c U^2 k^2}{\rho_s}\right)}}{\tanh kh + \rho_c/\rho_s} - \frac{2\nu_s k^2 \tanh kh}{\tanh kh + \rho_c/\rho_s} \quad (4.1)$$

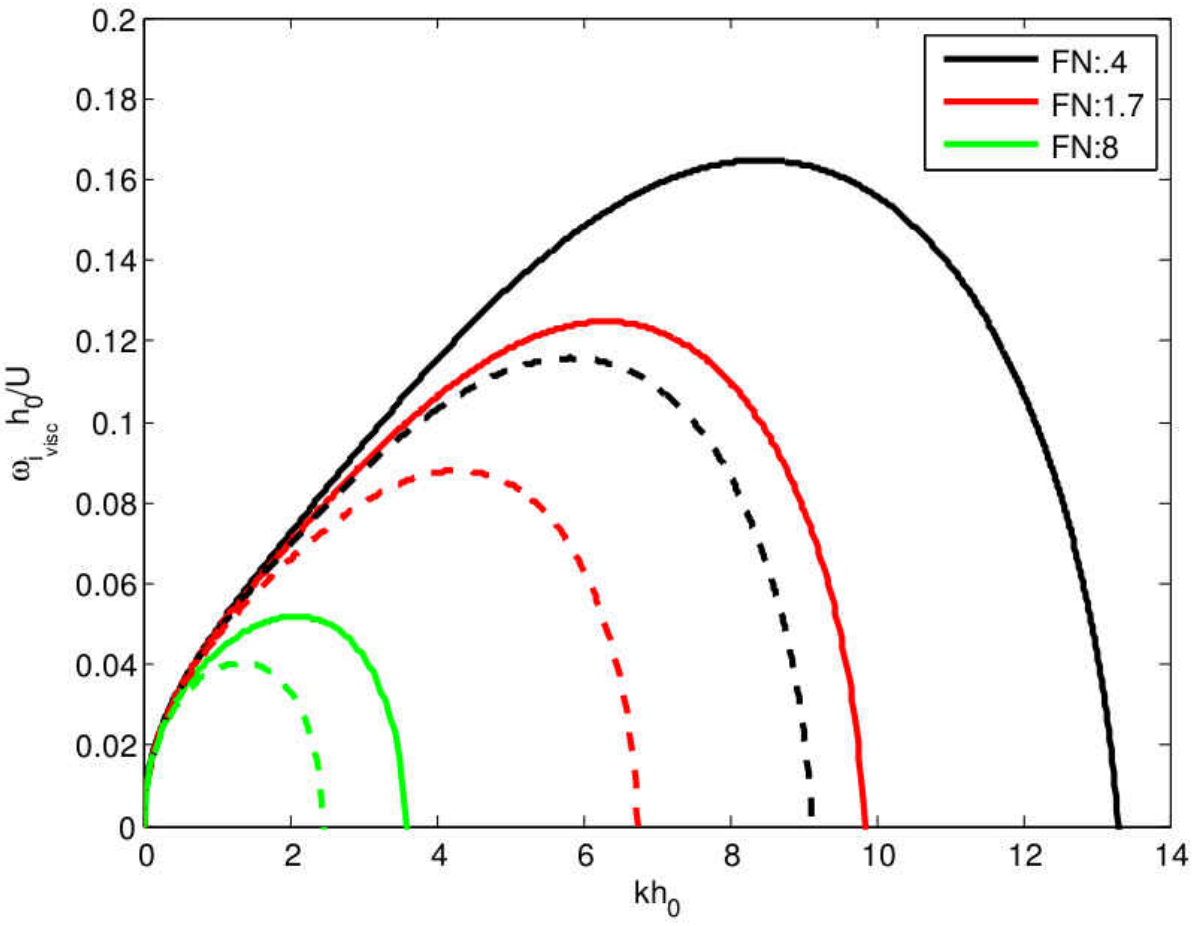

Figure 4.1: The temporal growth rate for $FN = .4, 1.7, 8$. The dotted line represents $\sigma = 70mN/m$ and the solid line represents $\sigma = 48mN/m$.

Two immediate observations can be made in Figure 5. First, the cut-off wave number (k-intercept) increases as flow number decreases. Secondly, the maximum growth rate increases as flow number decreases. Given that the cut-off wave number represents the upper bound for the domain of unstable waves, the first observation indicates that the smallest flow number will have the largest set of unstable waves. Also given that the maximum growth rate represents the mode of temporal instability, the second observation is that the smallest flow number will have the higher mode of instability. Therefore it is clear from Figure 5 that FN=.4 will have the greatest degree of

sheet instability and breakup. Moreover, we expect FN=.4 to have more sequences in cascading atomization process (see section 4.2). The effect of surface tension displays similar behavior to the flow number effect on growth rate. Therefore, there is a larger set of unstable waves and higher mode of instability as surface tension decreases.

In order to further evaluate the spray characteristics, the droplet diameter and velocities were measured with PDPA diagnostic system at a constant $Re \approx 21000$ and both $\sigma = 70mN/m, 48mN/m$ and for all three flow numbers (FN=.4,1.7 and 8).

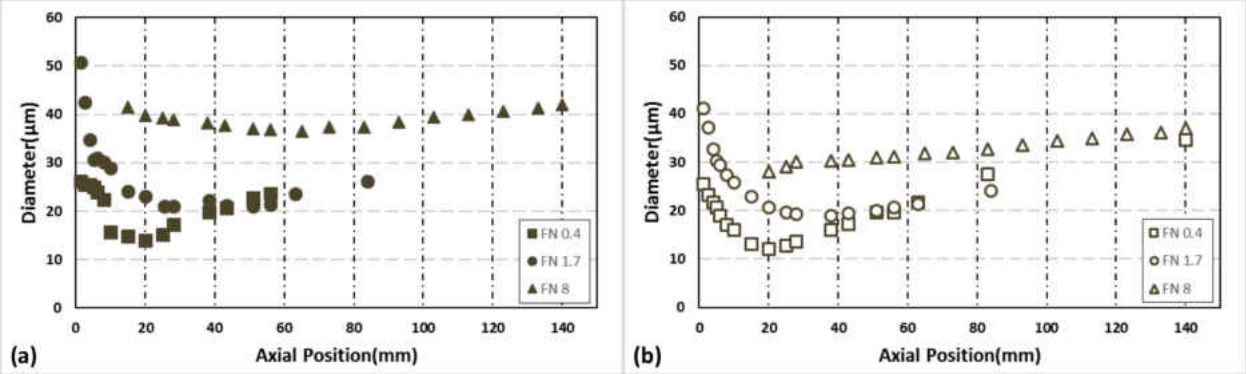

Figure 4.2: Average diameter profile for measured droplets along the axis with $Re = 21000 \pm 150$ (a) $\sigma = 70mN/m$ (b) $\sigma = 48mN/m$

From both figures 4.2 (a) and (b) it is displayed that for higher flow numbers, the droplet size is also higher. This is expected because as flow number increases, so does mass flow rate. Since the Reynolds number is being held constant, the velocity of sheet for higher flow numbers is smaller. Thus, with increasing flow number, the thickness of the liquid film increases which when disintegrated either through perforation or wave disintegration, produces larger droplets. As previously stated and observed from figure 4.1, the smallest flow number has the highest growth rate which means that it is also undergoing a higher mode of instability. Since the liquid sheet for the smallest flow number is undergoing a higher mode of instability, there will also be a higher

breakup mode occurring.

When comparing figures 4.2 (a) and (b) we see that with decrease in surface tension, the droplet size also decreases. This is due to the fact that secondary breakup is occurring at a higher frequency and coalescence is occurring less frequently. Another interesting observation is that the average diameter for the smallest flow rate FN=.4 increases at a higher rate further downstream than compared to FN=1.7 and FN=8. This due to the fact that at FN=.4 the coalescence is much higher further downstream than for larger flow numbers.

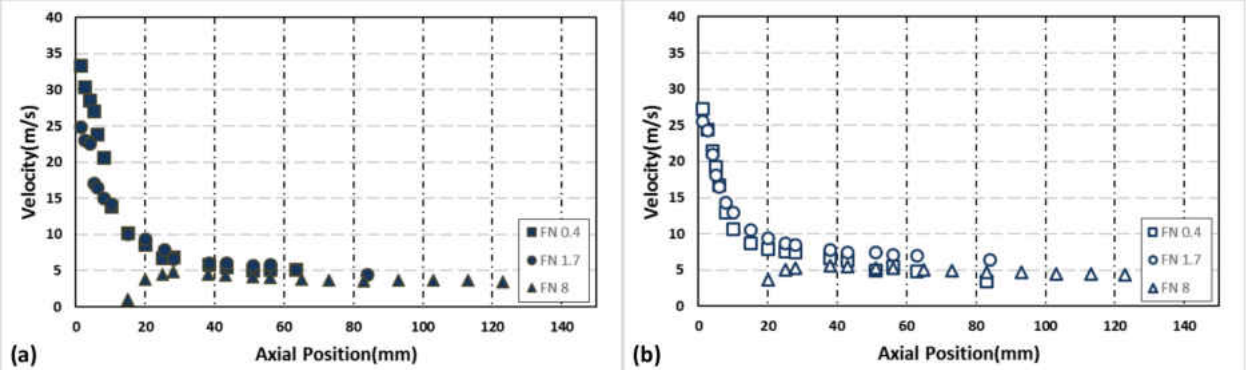

Figure 4.3: Average velocity profile of droplets along the axial position for $Re = 21000 \pm 168$. (a) $\sigma = 70mN/m$ (b)$\sigma = 48mN/m$

One unique observation, from figure 4.3 is that for FN=8, the velocity tends to increase before approaching asymptotic value. It is speculated this is due to the contribution of a recirculation regime, which was discovered to occur for $Re > 20,0000$ by Saha et al. (2012). Nevertheless, Figure 4.3 demonstrates the monotonically decaying behavior of the velocity. The velocity decreases due to the loss in kinetic energy from the secondary breakup process. Faeth et al. (1995) demonstrate the decrease in velocity, after breakup, through phenomenological and empirical analysis.

4.2 Secondary Breakup

In order to discuss the phenomena of secondary breakup, the physical context of where the secondary breakup occurs must also be discussed. In regards to the breakup regime of a hollow cone spray, secondary breakup is either ultimate or penultimate sequence of the cascading atomization process.

4.2.1 Cascade Atomization

In the primary breakup regime of a spray it is seen that Rayleigh Plateau Instability(RPI), Rayleigh Taylor Instability(RTI), Kelvin Helmholtz instability(KHI), and even turbulence are all mechanisms which compete against each other in order to induce breakup of a jet or film(Rimbert and Castanet 2011). However, that does not mean that if one instability mechanism occurs, the other instability mechanisms can be neglected. In fact, it is both experimentally and numerically observed that once one mode of instability occurs, other modes of instability follow, causing the cascading nature of atomization (Beale and Reitz 1999, Tanner 2004, Wang, Im et al. 2008, Park, Kim et al. 2009, Rimbert and Castanet 2011).

The significance of cascading nature in atomization can be further understood from the experiments of Wang, Im et al. (2008). Wang observed that at an air speed lower than 60 m/s (but higher than 45 m/s) Kelvin Helmholtz instability would manifest in the form of surface undulations on the jet causing ligaments to protrude from the surface, pinch off, subsequently retract and breakup due to capillary instability. At an air speed greater than 60 m/s Wang observed that instead of ligaments, the surface undulations were blown into two dimensional membranes with thick rims which would produce similar behavior to the bag breakup of a droplet where the residual rim would retract, coalesce and breakup due to capillary instability. The key observation here is that the residual

rim displayed behavior similar to the ligament. Additionally Theofanous (2011) has shown that the lower modes of droplet breakup such as bag and bag and stamen breakup, are actually caused by weak modes of RTI. This leads one to infer that because a stronger mode of KHI occurred on the surface of the jet, the subsequent breakup process went from RTI induced to capillary instability. Therefore it is important to understand the preceding instability in order to understand and describe the breakup criteria of secondary breakup regime.

4.2.2 Literature Search In Breakup Criteria

On the topic of breakup criteria, tremendous amount of research has been conducted by many in order to create a distinct critical point at which breakup occurs based on Weber number. Luna and Klikoff Jr (1967), Hsiang and Faeth (1992), Wierzba (1990), are just a few who give a detailed catalog of previous experiments(including the work of other researchers) and the critical Weber number determined from those experiments. To summarize, critical Weber number at which onset of breakup occurs varies greatly from as low as 1 to as high as 60. There are three major factors which alter critical Weber number and lead to such large variance in its calculation. First, the viscosity of the liquid globule or droplet has a dampening effect on the oscillation and deformation, thus more viscous droplets require a stronger external force or Weber number to induce breakup. Secondly, since RTI is a primary mechanism governing the breakup of a droplet (Beale and Reitz 1999, Theofanous 2011), then the density ratio between droplet and the continuous phase must be taken into account. Duan, Koshizuka et al. (2003) developed a relationship for critical Weber number dependency on density ratio using numerical results from simulation. Lastly, the flow regime of the continuous phase and /or the presence of flow disturbances have shown to alter the critical breakup Weber number (Blanchard 1950, D'albe and Hidayetulla 1955, Luna and Klikoff Jr 1967, Theofanous, Li et al. 2007).

To summarize, critical Weber number at which onset of breakup occurs varies greatly from as low as 1 to as high as 60. There are three major factors which alter critical Weber number and lead to such large variance in its calculation. First, the viscosity of the liquid globule or droplet has a dampening effect on the oscillation and deformation, thus more viscous droplets require a stronger external force or high Weber number to induce breakup. Secondly, since RTI is a primary mechanism governing the breakup of a droplet (Beale and Reitz 1999, Theofanous 2011), then the density ratio between droplet and the continuous phase must be taken into account. Duan, Koshizuka et al. (2003) developed a relationship for critical Weber number dependency on density ratio using numerical results from simulation. Lastly, the flow regime of the continuous phase and /or the presence of flow disturbances have shown to alter the critical breakup Weber number (Blanchard 1950, D'albe and Hidayetulla 1955, Luna and Klikoff Jr 1967, Theofanous, Li et al. 2007).

Table 4.1: Secondary breakup modes which occur when $Oh < .1$. This table was compiled from the observations and data of Guildenbecher et al. (2009), andTheofanous and Li (2008).

Breakup Mode	Range of We_d
Vibrational deformation	$0 < We_d < 11$
Bag, Bag and Stamen (Rayleigh Taylor Piercing)	$11 < We_d < 35$
Multimode (Rayleigh Taylor Piercing)	$35 < We_d < 80$
Sheet-thinning	$80 < We_d < 350$
Shear-Induced Entrainment with Rupture	$We_d > 350$

4.2.3 New Breakup Model and Criteria

In the current experiment, the majority of the droplets have an Ohnesorge number less than .1 and less than 1 percent of all the droplets for all cases have $We > 12$. As previously mentioned the cascading nature of breakup and flow conditions are both important factors in determining the breakup of the droplet. For all three Flow Numbers, the hollow cone sheet breakup is governed by either transitional long wave to short wave Kelvin Helmholtz unstable instability or short wave dominant Kelvin Helmholtz instability. Also, the measurements of the droplets were taken either just inside the cone and/or near breakup of the film. Thus the fluctuations in pressure and velocity caused by the propagating surface waves on the film contribute to flow disturbances in the spatial location where the droplets were measured.

With both of these observations considered, we can deduce that the breakup of the droplet is due to the combination of Rayleigh Taylor instability and capillary instability (in the case of short wave dominant breakup of the film) and capillary instability (in the case of transitional long wave to short wave breakup of the film).

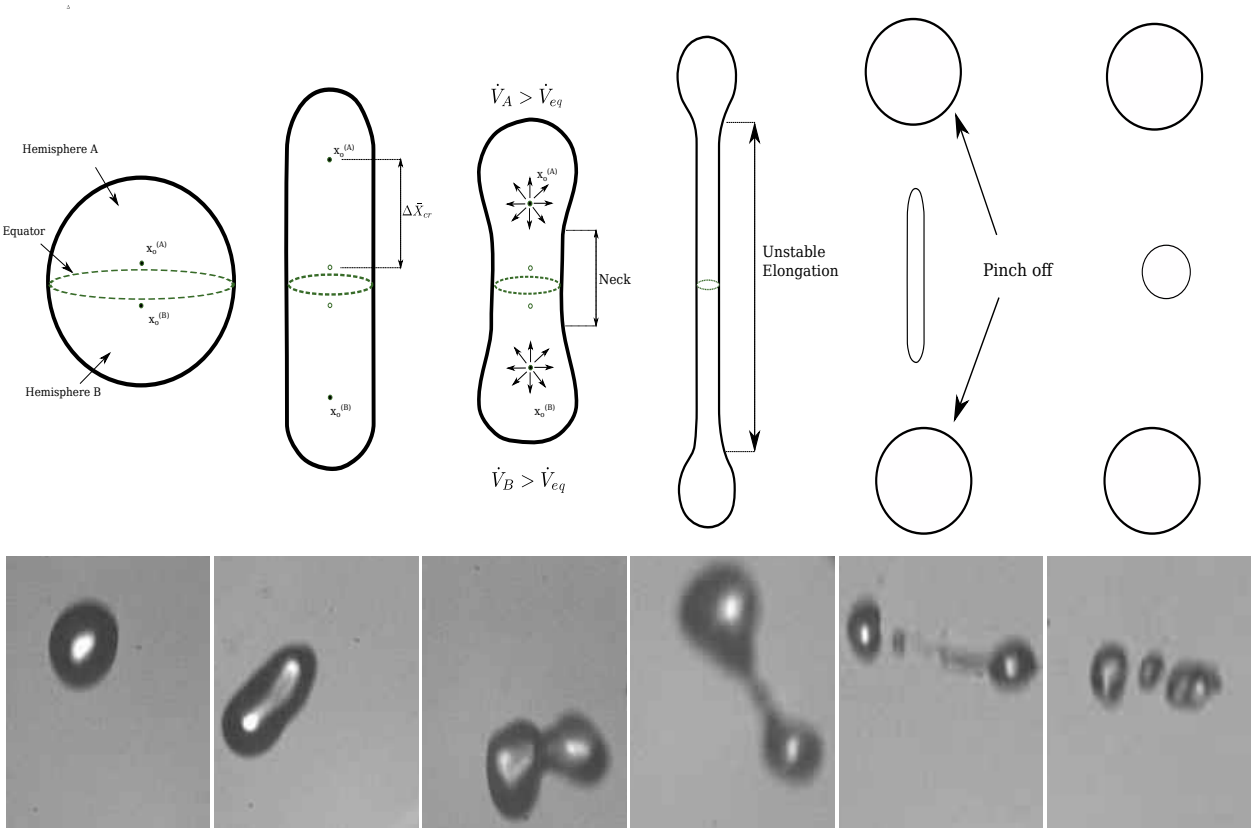

Figure 4.4: Comparison of the phenomenological breakup model with experimentally observed images. All images were taken at a frame rate of 100,0000 at $Re \approx 40A$ for FN=.8 droplet is initially stable but eventually elongates. Instead of restoring to a spheroid, the droplet resembles a dumbbell structure. Consequently, the dumbbell-shaped sphere starts restoring closer to the poles than the equator. This results in further unstable elongation which leads to pinch off.

From a phenomenological standpoint, breakup due to vibrational breakup can be considered a capillary instability. A droplet oscillating due to external aerodynamic forces will distort become prolate and then restore back to spherical shape due to surface tension acting as a restoring force. In the case of vibrational breakup, center of mass of the half prolate droplet is shifted a critical distance away from the equilibrium position such that when the droplet begins to restore its shape, dilation occurs faster at the opposite poles than the equator of the flattened prolate droplet. The droplet begins to create a dumbbell like structure and a neck bridge begins to develop at between

the two dilating poles of the droplet. After a certain point, the neck bridge becomes unstable and pinches off, hence breakup by capillary instability (Marmottant and Villermaux 2004). This model is shown in figure 4.4.

From Table 4.1 it would appear that bag burst would not be possible since the Weber number is below 12. However as previously mentioned, there are flow disturbances caused by the film would induce a higher mode of breakup. Koenig (1965) visually displayed drops that would normally breakup by vibrational deformation, breakup by bag bursting when exposed to the wake of another droplet. Moreover, not only fluctuations from the film, but also the presence of other droplets can promote bag burst of droplets near the breakup regime of the film.

Therefore, while capillary instability of droplets is occurs in the cascade sequence, bag burst breakup of droplets is still possible due to the kinematics of the continuous phase. With the governing mechanism of secondary breakup restricted to both bag bursting and vibrational modes, Clark's model for breakup was used to calculate the theoretical deformation of each droplet. Like the TAB model, Clark modeled the forces acting on the droplet(external aerodynamic force, viscous dissipation force, restoring surface tension force) using the Taylor analogy of a spring dash pot system (O'Rourke and Amsden 1987, Clark 1988). Unlike the TAB model, Clark uses the spring dash pot analogy to track the distortion of the center of mass of the half droplet. This distinction allows for analogies to be drawn with the phenomenological model shown in figure 4.4. In addition, the equations for all three forces were recovered from energy balance, which allows physical interpretation of the physical parameters of our experiment. The advantage of Clark's model is that it accounts for drop deformations occurring at both poles and the forces are applied through the center of mass of the isotropic drop (Clark 1988, Ibrahim, Yang et al. 1993, Lee, Park et al. 2012).

The non-dimensional form of Clark's model is:

$$(K+1)\ddot{y} + \frac{9\pi(N+1)}{4Re_d}\dot{y} + \frac{9\pi^2}{4We_d}\left(y - \frac{4}{3\pi}\right) = \frac{2}{\pi} \tag{4.2}$$

Where $K = \frac{\rho_c}{\rho_d}$, $N = \frac{\mu_c}{\mu_d}$, $Re_d = \frac{\rho_c u r_0}{\mu_c}$, $We_d = \frac{\rho_c u^2 r_0}{\sigma}$, $t^* = \frac{tu}{r_0}$, $y^* = \frac{4a}{3\pi r_0}$. Note the * were dropped from the non-dimensional variables, for the sake of brevity. By solving the characteristic equation, equation 4.2 can be analytically determined to yield:

$$y = \frac{4(3\pi^2 + 2We_d}{9\pi^3} + e^{-\frac{9\pi^2(N+1)}{8Re_d(K+1)}t}\left(C_1 \sin\omega_d t + C_2 \cos\omega_d t\right) \tag{4.3}$$

$$C_1 = y_0 - \frac{4(3pi^2 + 2We)}{9\pi^3} \tag{4.4}$$

$$C_2 = \frac{\dot{y_0}}{\omega_d} + \frac{(N+1)(9\pi^3 y_0 - 8We_d - 12\pi^2)}{8\pi Re_d(K+1)\omega_d} \tag{4.5}$$

$$\omega_d = \frac{3\pi}{8Re_d}\sqrt{\frac{16Re_d^2(K+1) - 9\pi^2 We_d(N+1)^2}{We_d(K+1)}} \tag{4.6}$$

The initial conditions are $y_0 = \frac{4}{3\pi}$ and $\dot{y} = 0$. It is important to note that Clark's model linearizes the viscous dissipation force and restoring force due to surface tension. Since we are restricting the use of the model within the vibrational deformation mode and onset of bag breakup where deformation(displacement of center mass of the half droplet) are small, the residual error accrued from neglecting the nonlinear terms should not be high.

The breakup criteria chosen for our data is a modified version of TAB model's breakup criteria. The modification allows us to incorporate droplets that breakup due to vibrations as well as bag bursting. It is observed that breakup has a chance to occur if the deformation of the droplet exceeds that of the maximum stable cross-stream diameter. Hsiang and Faeth (1992) developed an

empirical correlation for ratio of maximum cross-stream diameter over original undisturbed diameter of the droplet for droplets undergoing vibrational deformation without breakup. If we assume the deformation to be equal at both poles of the droplet, equation 4.7 can be used to calculate the maximum stable elongation over the unperturbed radius of the droplet.

$$\left(\frac{a}{r_0}\right)_{maxstable} = 1 + .19\sqrt{We_d} \tag{4.7}$$

However, the deformation of the droplet exceeding the maximum stable deformation is not enough to conclude breakup will occur. This conclusion was made by Wierzba (1990). He observed that the deforming droplets reach the onset of vibrational breakup but yet revert back to stable droplets. Therefore, droplets that approach the onset of vibrational breakup have the possibility to restabilize their shape without breaking up. In order to distinguish between droplets that successfully undergo vibrational breakup and droplets that fail to undergo vibrational breakup, the theoretical breakup time was obtained. If the theoretical breakup time is less than the period of oscillation, then vibrational breakup will successfully occur.

$$t_{osc} = \frac{2\pi r_0}{\omega_d u} \tag{4.8}$$

$$t_b = \frac{r_0}{u}\sqrt{\frac{4\rho_d}{3\rho_c}\left(\frac{\delta}{r_0}\right)_{crit}} \tag{4.9}$$

Table 4.2: Breakup criteria used to determine the breakup occurrence of a droplet.

Event		Probability
A	$\left(\frac{a}{r_0}\right)_{maxstable} < \frac{3\pi}{4} y_{max}$	$P(A) = \frac{Droplets\ undergoing\ Event\ A}{Total\ number\ of\ droplets}$
B	$t_b < t_{osc}$	$P(B\|A) = \frac{Droplets\ undergoing\ Event\ B\ and\ A}{Droplets\ undergoing\ Event\ A}$
C	$Breakup\ of\ Droplet$	$P(C) = P(A) \bigcap P(B\|A)$

Oscillation time (equation 4.8) is derived from the angular frequency of the Clark model as shown in equation 4.6. It is important to note that since time was non-dimensionalized, t_{osc}, is multiplied by $\frac{r_0}{u}$ in order to recover the dimensional time.

Hinze's (1949) derivation for breakup time t_b was used in equation 4.9. $\left(\frac{\delta}{r_0}\right)_{crit}$ is chosen to be one.

Table 4.2 summarizes the modified breakup criteria. Event A is the event that a droplet's radial distortion is greater than the maximum stable distortion. $\left(\frac{a}{r_0}\right)_{maxstable}$ is calculated using equation 4.7, where y_{max} is calculated from equation 4.3 by numerically finding the maximum value of y . Also note that since y is measured from the center of the half hemisphere, it is therefore rescaled in event A to represent the distortion which would occur at the pole of the droplet. Event B is the event that the breakup time is less than the period of oscillation. Event C is the union of Event A and B, therefore the probability of event C is the probability of breakup. Note that a droplet which undergoes bag bursting, successfully undergoes event C as well. Hence, the proposed breakup

criteria predict the probability of droplets undergoing both vibrational breakup and bag bursting.

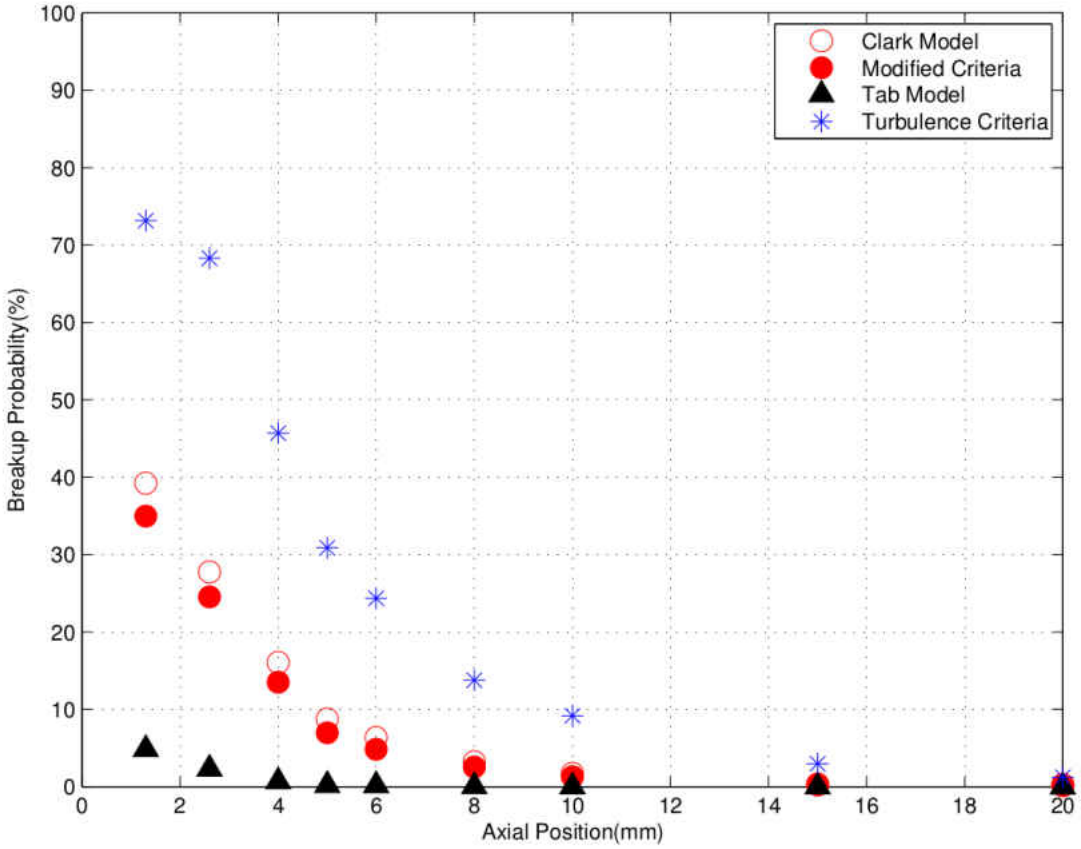

Figure 4.5: The breakup probability along the axis $FN = 1.7$ $Re \approx 21000$ $\sigma = 48mN/m$. Clark's Model refers to the probability of event A (shown in Table 4.2 occurring. Modified criteria refers to the probability of event C (also shown in Table 4.2 occurring. Tab model refers to the breakup criteria proposed by Reitz ($We_d > 6$). Turbulence criteria refers to the breakup due to high turbulence intensity ($We_d > 1.5$) which is based on the work of D'Albe and Hidayetulla(1955) and Blanchard(1950).

From figure 4.5 we see that the modified criteria predicts breakup to occur at a probability between that of the TAB model and Turbulence Criteria. This correlates well with our experimental results. The TAB model only predicts droplet which breakup only by bag breakup or higher modes while neglecting breakup due to vibrational deformation. Thus, TAB model would under predict

breakup when vibrational deformation is the prime mode of breakup. The Turbulence criteria assume a high intensity of turbulence is present. While the velocity fluctuations induced by the waves propagating in the liquid sheet are a source for turbulence intermittency, we suspect the turbulence to be dissipative some near the axial location. Therefore the turbulence intensity should be less near the axial location and the breakup should be less than that predicted by the Turbulence criteria. Regardless of the breakup criteria we see that the breakup probability monotonically decreases in the downstream direction. Another important observation is that once breakup probability reaches zero it remains zero. This is expected given that breakup is cascading in nature and secondary breakup is the last stage of breakup. Moreover, the breakup probability is only significant in the near field region where the conical liquid film breakup is occurring.

4.2.4 Breakup Analysis

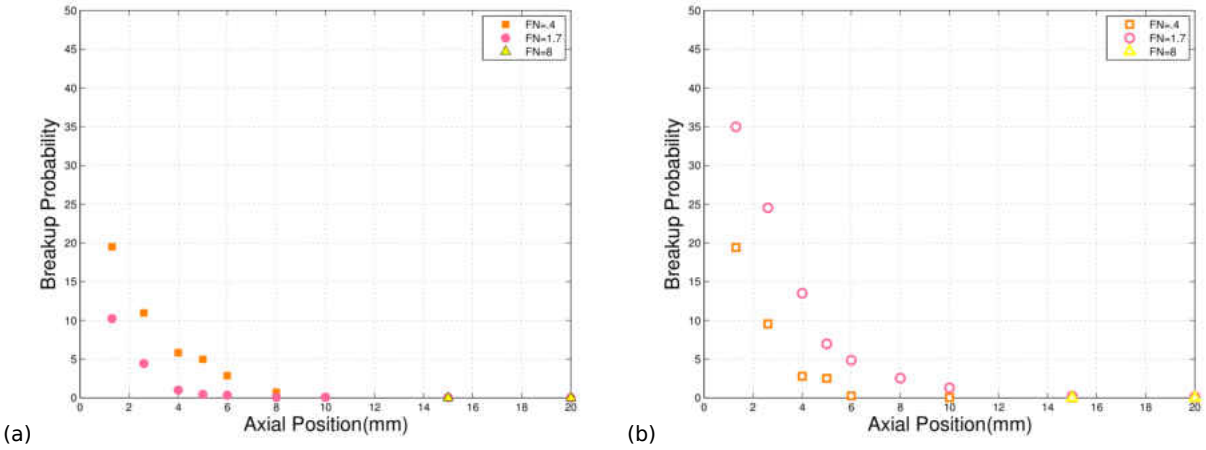

Figure 4.6: The breakup probability along the axis , for different axial positions. All data points on both (a) and (b) were calculated using the modified criteria. (a) For $FN = .4$,$FN = 1.7$,$FN = 8$, with $\sigma = 70mN/m$, $Re \approx 21000$. (b) For $FN = .4$,$FN = 1.7$,$FN = 8$, with $\sigma = 48mN/m$, $Re \approx 21000$.

When comparing the breakup probability between two liquids with two different surface tensions we see that a decrease in surface tension increases the probability of secondary breakup. This increase in breakup probability can be observed when looking at the difference between figure 4.6 (a) and figure 4.6(b). Since surface tension acts as a stabilizing force, the decrease in surface tension allows the tangential component of velocity acting along the liquid film to induce faster growing waves. The faster growing waves tend to break off the liquid sheet quicker forming more blob-shaped fragments (instead of slender ligaments) which tend to undergo bag bursting mode of breakup instead of going straight to vibrational breakup. Thus, despite the information displayed in Table 4.1 , bag bursting mode is occurring because the liquid film undergoes a more dominant mode of short wave Kelvin Helmholtz instability causing a cascading effect which leads to bag bursting mode and ultimately to vibrational breakup of the bursted bag's rim.

Another observation that can be seen is that the breakup is the highest for the nozzle with the smallest flow number (FN= 0.4). This is expected because cone angle is small and the axial location is not far from the radial location where the periphery of the conical liquid film is breaking up due to unstable Kelvin Helmholtz short waves. For the largest flow rate (FN= 8), there seems to be no breakup occurring at all near the axis regardless of surface tension effects. This is due to cone angle being large and that the axial location is significantly far away from the periphery of the conical liquid film and that the cascading breakup process has reached completion.

4.3 Coalescence

Due to the stochastic nature of droplet formation caused by cascading breakup, droplets within the hollow cone spray are bound to collide, bounce, coalesce, or split. Qian and Law (1997),Jiang, Umemura et al. (1992) determined that there is a critical amount of kinetic energy required to overcome viscous dissipation during collision in order for two colliding droplets to split up again.

The critical kinetic energy can be described by the We_{crit}, which can be found from equation 4.10 where Saha et al. (2012) demonstrated that a first order conservative estimate of the coalescence probability in a hollow cone spray can be found if we assume head on collisions only (impact parameter B=0). Therefore, the coalescence probability for that a droplet has is when the collision Weber number is $We_l = \frac{\rho_d U_{rel}^2 d_0}{\sigma}$.

$$We_{crit} = 30Oh_{col} + 15 \tag{4.10}$$

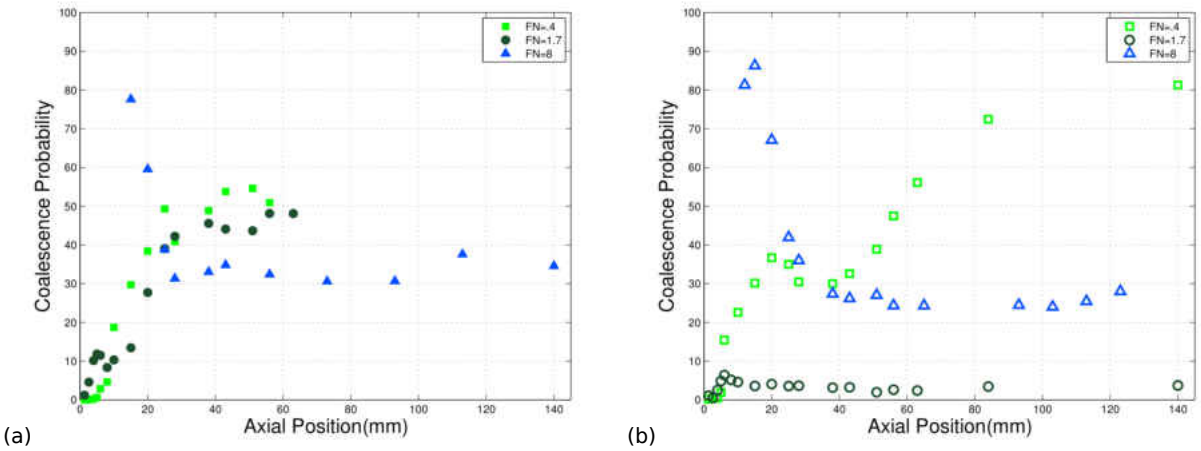

Figure 4.7: Coalescence probability for all three flow numbers along the axis, in the downstream direction. (a) For $FN = .4, FN = 1.7, FN = 8$ with $\sigma = 70mN/m$, $Re \approx 21000$. (b) For $FN = .4, FN = 1.7, FN = 8$ with $\sigma = 48mN/m$, $Re \approx 21000$.

Contrary to the breakup probability, a decrease in surface tension causes a decrease in coalescence, as shown in figure 4.7 (a) and (b). When two droplets collide, they begin to oscillate between the shape of a newly coalesced droplet and a stretched ligament at the onset of breaking up (Qian and Law 1997). Since surface tension acts as a restoring force when a droplet (or two colliding droplets) is oscillating, a decrease in surface tension allows the colliding droplets to oscillate further away from equilibrium spheroid shape and into an even more stretched ligament. Longer

and slender ligaments have a higher chance of breaking up, thus a lower probability of coalescing.

Another difference between breakup probability and coalescence probability, is that the coalescence probability displays more of a dynamic behavior as shown in figure 4.7. Particularly, we see in the near field region (axial position $< 20mm$) there is a sharp increase in coalescence probability. This is could be due to the fact that after droplet has undergone a mode of breakup, there are always fragmented membranes associated with the breakup that tend to coalesce into either a droplet or a slender ligament which undergoes capillary instability. A statistical explanation can be given by observing figure 4.8.

Scaling We_{col} with We_{crit} the critical condition for coalescence is found to occur when $\frac{We_{col}}{We_{crit}} < 1$. In this manner, we can examine the migration of the scaled pdf distribution. Figure 4.8 displays the migration of the scaled pdf distribution for case of $FN = 4,\ \sigma = 48mN/m,\ Re \approx 21000$. After primary breakup, the droplets formed have a very large amount of kinetic energy such that coalescence becomes insignificant, as shown in figures 4.8 (a),(b),(c). Due to the secondary breakup of droplets, the velocity and kinetic energy associated with each droplet is less for every daughter droplet produced. This loss in kinetic energy exhibits a decrease in the collision kinetic energy causing the pdf to not only migrate but to also converge towards the critical kinetic energy required as shown in figures 4.8 (a),(b),(c),(d),(e),(f). The pdf convergence at 1 occurs due to the fact that droplets that have already broken up will not breakup again, thus remain the same with kinetic energy less than the critical kinetic energy. Once cascading breakup has finished the velocity of the droplets reach a terminal value. Further downstream, droplets with near critical kinetic energy are being depleted from the axial center and pulled towards the periphery. This occurs because of the centrifugal dispersion displaces larger droplets toward the periphery (Saha, Lee et al. 2012). This causes the flattening of the pdf, seen in figure 4.8 (g),(h),(i). With smaller droplets further downstream, viscous dissipation becomes more dominant causing the critical kinetic energy required for splitting to increase. With this steady increase in critical kinetic energy, the pdf begins

to steadily migrate below the critical line (1) as seen in figure 4.8 (j), (k), (i).

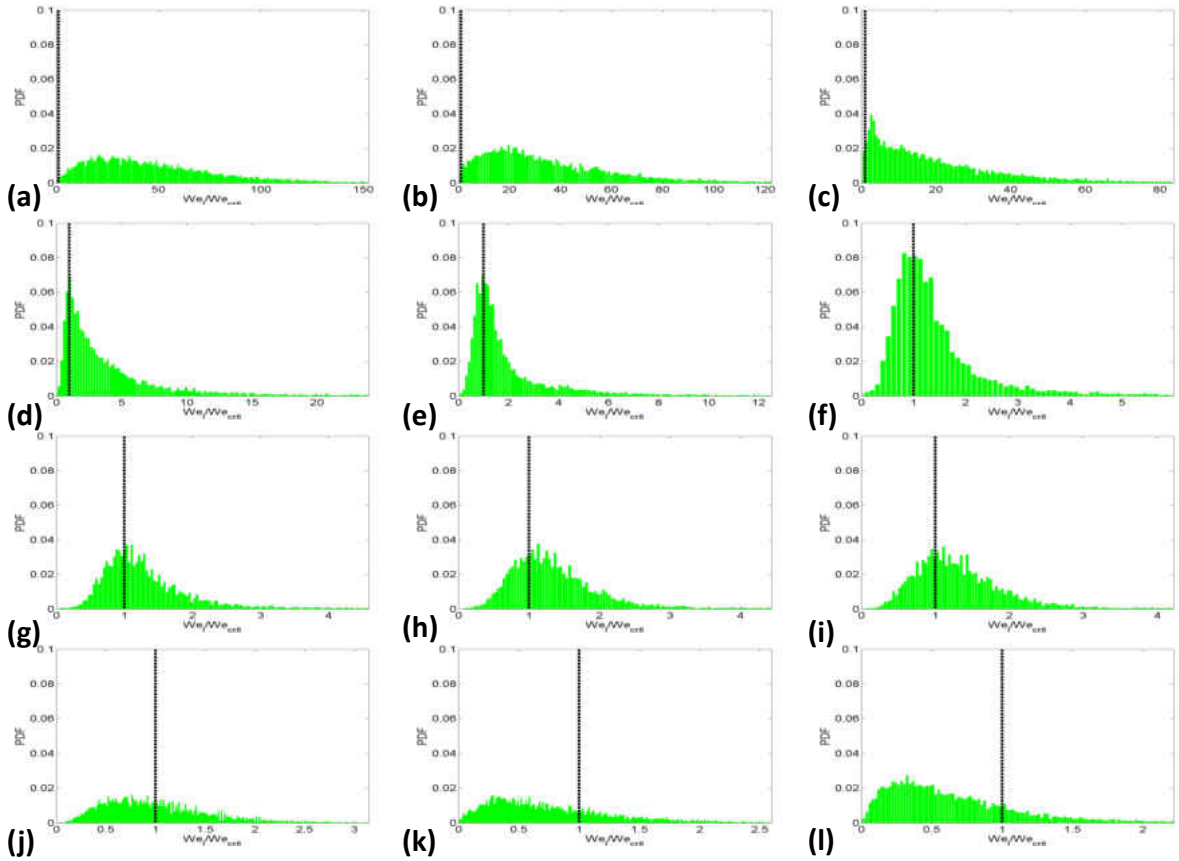

Figure 4.8: Coalescence migration for $\frac{We_l}{We_{crit}}$ A critical line is displayed at 1, for all sub figures, indicating the criteria for coalescence,$\frac{We_l}{We_{col}}$. For axial positions (a) 1.3mm, (b) 2.6mm, (c) 5mm, the pdf is moving closer to the critical line. For axial positions (d) 10mm, (e) 15mm, (f) 20mm, The pdf begins to converge onto 1. For axial positions (g) 25mm, (h) 38mm, (i) 43mm, the pdf begins to redistribute and flatten out evenly. For axial positions (j) 51mm, (k) 84mm, (l) 140mm, the pdf migrates below the critical line.

With an understanding of the dynamic behavior of coalescence, figure 4.7 (a) and (b) indicates coalescence probability for FN=1.7, the sharp coalescence is much less than that of FN= .4; where coalescence probability is the probability that a droplet has a We_l less than We_{crit}. This is due to

the fact that for FN=.4, there is much higher collision frequency leading to a higher probability. Moreover, figure 4.7 (b) shows that further downstream, FN= .4 coalescence probability continues to increase, while FN= 1.7 and FN=8 remain constant. For FN= .4, the axial component of velocity is the most dominant component so droplets moving downstream are not being pushed towards the periphery as much in the case of FN= 1.7 and FN= 8. Coupled with the high frequency of collisions, a continuous increase in coalescence is a plausible outcome.

Despite this agreement of FN=1.7 and FN=.4 with the dynamic behavior described by figure 4.8, FN=8 seems to have a distinct behavior pattern. In particular FN=8 has a much larger coalescence probability near $z = 15mm$. From chapter 4, it was shown that at $Re \approx 21000$, there is not much excess swirl given by the nozzle with FN=8. Also the film rupture occurs $\approx 10mm$ for this case as well. Therefore, the swirling liquid film is in a meta-stage where it is neither a fully developed cone nor a collapsed sheet. From morphological examination of the sheet, protruding ligaments can be seen to form. Therefore the higher coalescence probability is likely occurring due to ligaments simultaneously stretching and recessing into a larger globule.

An interesting observation between figure 4.7 (a) and (b) is that for water (figure 4.7 (a)) FN=8, remains constant at a lower coalescence probability downstream than that of FN=1.7, but for (figure 4.7 (b)) FN=8 remains constant at a higher coalescence probability than that of FN=1.7. Further examination of FN=8 shows that there actually is not much of a decrease in coalescence probability caused by the decrease in surface tension.

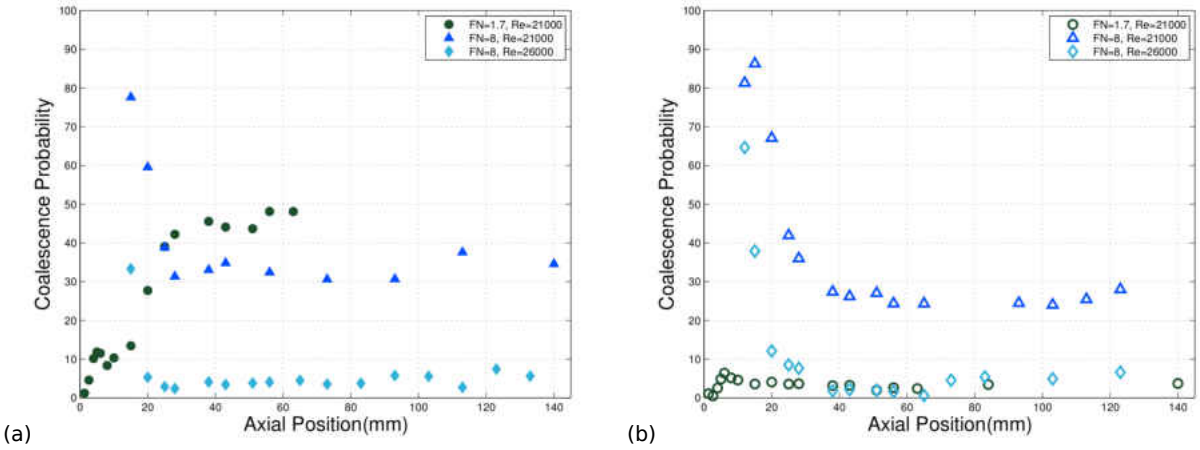

Figure 4.9: The coalescence probability for all three flow numbers along the axis in the downstream direction. (a) For $FN = 1.7,\ and Re \approx 21000,\ FN = 8\ and\ Re \approx 21000,\ FN = 8 Re \approx 26000$, with $\sigma = 70 mN/m$. (b) For $FN = 1.7,\ and Re \approx 21000,\ FN = 8\ and\ Re \approx 21000,\ FN = 8 Re \approx 26000$, with $\sigma = 48 mN/m$.

This peculiarity can be attributed to FN=8 at is underdeveloped flow displaying onion/tulip zone features, for both water and $\sigma = 48 mN/m$. If we examine FN=8 at a higher Reynolds number ($Re \approx 26000$), we see that FN=8 actually has the less or approximately the same coalescence as FN=1.7, as shown in figure 12.

In summary, it can observed that both breakup and coalescence contribute to the diameter profile in a hollow cone spray. As breakup probability monotonically decreases, coalescence probability shows a sharp increase before decaying due to centrifugal dispersion. It is speculated that the time scale at which coalescence occurs is much slower than the breakup time scale. Thus for droplet size to increase due to coalescence, the probability of of coalescence must be much larger than breakup probability. This region is clearly scene when compared to both the diameter and velocity profile for FN=.4 and FN=1.7. For the case of FN=8, there appears to be no breakup but high coalescence probability. However, due to the slower time scale of coalescence, droplet size does not increase until some axial distance downstream.

CHAPTER 5: CONCLUSION

The swirling liquid film emanating from three different pressure swirl atomizers with different flow numbers were studied. This study allowed for the further investigation of the dynamic behavior the swirling film and droplet and droplet/flow field interactions which gives insight to the cascading nature of the pressure-swirl atomization process. Ultra-speed imaging was conducted to obtain wavelength, film length, cone angle measurements for varying Reynolds Number between 10,000 70,000 and varying Weber Numbers between 1 15. Additionally, the localized droplet characteristics were analysed as well. The localized droplet characteristic profile is beneficial to the design of combustion chambers, where flame placement and dense droplet regimes are key factors leading to the optimization of combustion. Reynolds number was held constant at Re 21,000 for the droplet analysis for PDPA.

From the investigation of the swirling film, both the swirling behavior and sheet characteristics were determined. The swirling behavior of the liquid film is determined by the centrifugal force which is generated from the inertia of the film. Remarkably, the intrinsic behavior of film breakup or atomization is found to be governed by the centrifugal force or swirl intensity. Specifically, the atomization process changes from Rayleigh plateau instability, to rim disintegration and eventually to wave disintegration. Further investigation of the swirl strength or swirl parameter demonstrate that for increasing flow number or orifice number, there is a larger domain where the swirl is not stabilized. In other words, an increase in orifice diameter also leads to the requirement of a higher operating We condition to ensure a fully developed cone. Therefore, despite a larger orifice diameter leading to a larger range or Reynolds Number, the required operating Reynolds Number to ensure a conical film is also increased.

To corroborate film breakup phenomena, further insight into the temporal instability of the

attenuating liquid film was obtained. This was obtained from examination of the asymptotically large wavelength for a liquid film thickness, compared with the maximum wavelength measured on the surface of the swirling liquid film. Both the experimentally measured wavelengths and the theoretical wavelength compared well. This result further elucidates the ongoing debate of whether temporal instability exists or if spatial instability is sole contributor to the breakup phenomena in liquid sheet atomization. In other words, temporal instability does exist within a liquid sheet and manifest as the maximum wavelength, longest wavelength, on the surface of the liquid sheet. Additionally, this result allows for an accurate linear simplification of the interface of the liquid sheet which can be used to deterministically analyse the droplet profile near the film disintegration and ligament rupture regime.

In regards to wavelength measurements, the breakup length scale displays a piecewise behavior for varying Reynolds Number and Weber Number. This tendency is analogous to the capillary instability regime, first wind-induced regime, second wind-induced regime, fully developed atomization regime for a jet delineated by Reitz and Bracco (1982). In the case of a swirling liquid sheet the regimes are separated as such: a) long-wave dominant breakup mode where both capillary instability and Kelvin Helmholtz instability contribute to the breakup, b) short-wave dominant breakup mode where short Kelvin Helmholtz waves are the primary contributor to breakup, and lastly c) shear-induced breakup.

The droplet diameter and velocity profile measured for all three nozzles, showed agreement with the results obtained by Saha et al. (2012). Specifically, just downstream of the film rupture, there exists a regime where secondary breakup occurs, and further downstream there exists a regime where coalescence occurs.

Droplet breakup is confirmed to exist as consequence of the cascade atomization. Clark's model was used to analyze the breakup in the lower Weber number limit($We_d < 12$). Clark's model

allows for the possibility of both capillary instability and bag bursting breakup to occur.

The analysis obtained from the use of Clark's Model led to profound discovery. In particular, it was observed that the near axis breakup probability decreased for increasing flow number or orifice diameter. Conversely, the breakup probability becomes more prominent near the periphery of the hollow cone for increasing orifice diameter. This profound implication leads to additional constraints when considering geometrical design of combustion chambers. However, the secondary breakup becomes more prominent towards the periphery of the cone. Furthermore from cross examination, the secondary breakup regime is correlated with the location of smallest droplet sizes.

Lastly, the coalescence analysis also led to further significant considerations to geometry design. From the coalescence probability it was shown that for the smallest orifice diameter there is a steady increase in coalescence along the axis. Additionally, one way coupling is observed where only breakup effects coalescence. Nevertheless, both the breakup and coalescence analysis leads to significant considerations for the design of combustion chambers.

This study provides valuable insight to the cascading nature of pressure swirl atomization. Moreover, the understanding of cascade atomization leads to better insight into vaporization characteristics and future enhancement of combustion with particular focus on biofuel combustion.

LIST OF REFERENCES

[Acrivos and Lo, 1978] Acrivos, A. and Lo, T. (1978). Deformation and breakup of a single slender drop in an extensional flow. *Journal of Fluid Mechanics*, 86(04):641–672.

[Albrecht, 2003] Albrecht, H.-E. (2003). *Laser Doppler and phase Doppler measurement techniques*. Springer Science Business Media.

[Alekseenko et al., 1999] Alekseenko, S., Kuibin, P., Okulov, V., and Shtork, S. (1999). Helical vortices in swirl flow. *Journal of Fluid Mechanics*, 382:195–243.

[Ashgriz, 2011] Ashgriz, N. (2011). *Handbook of atomization and sprays: theory and applications*. Springer Science Business Media.

[Ashgriz and Mashayek, 1995] Ashgriz, N. and Mashayek, F. (1995). Temporal analysis of capillary jet breakup. *Journal of Fluid Mechanics*, 291:163–190.

[Baranger, 2004] Baranger, C. (2004). Modelling of oscillations, breakup and collisions for droplets: the establishment of kernels for the tab model. *Mathematical Models and Methods in Applied Sciences*, 14(05):775–794.

[Beale and Reitz, 1999] Beale, J. C. and Reitz, R. D. (1999). Modeling spray atomization with the kelvin-helmholtz/rayleigh-taylor hybrid model. *Atomization and sprays*, 9(6).

[Berthoumieu et al., 1999] Berthoumieu, P., Carentz, H., Villedieu, P., and Lavergne, G. (1999). Contribution to droplet breakup analysis. *International journal of heat and fluid flow*, 20(5):492–498.

[Blanchard, 1950] Blanchard, D. C. (1950). The behavior of water drops at terminal velocity in air. *Transactions, American Geophysical Union*, 31:836–842.

[Bremond et al., 2007] Bremond, N., Clanet, C., and Villermaux, E. (2007). Atomization of undulating liquid sheets. *Journal of Fluid Mechanics*, 585:421–456.

[Carvalho et al., 2002] Carvalho, I., Heitor, M., and Santos, D. (2002). Liquid film disintegration regimes and proposed correlations. *International journal of multiphase flow*, 28(5):773–789.

[Chou et al., 1997] Chou, W., Hsiang, L., and Faeth, G. (1997). Dynamics of drop deformation and formation during secondary breakup in the bag breakup regime. *AIAA Paper*, (97-0797).

[Chou and Faeth, 1998] Chou, W.-H. and Faeth, G. (1998). Temporal properties of secondary drop breakup in the bag breakup regime. *International Journal of Multiphase Flow*, 24(6):889–912.

[Chryssakis et al.,] Chryssakis, C., Assanis, D., Lee, J., and Nishida, K. An investigation of the breakup mechanisms for swirl sprays from high-pressure swirl injectors. In *9th International Conference on Liquid Atomization and Spray Systems, Sorrento, Italy*.

[Clanet and Villermaux, 2002] Clanet, C. and Villermaux, E. (2002). Life of a smooth liquid sheet. *Journal of fluid mechanics*, 462:307–340.

[Clark and Dombrowski, 1972] Clark, C. and Dombrowski, N. (1972). Aerodynamic instability and disintegration of inviscid liquid sheets. *Proceedings of the Royal Society of London. A. Mathematical and Physical Sciences*, 329(1579):467–478.

[Clark, 1988] Clark, M. M. (1988). Drop breakup in a turbulent flow—i. conceptual and modeling considerations. *Chemical engineering science*, 43(3):671–679.

[Crapper et al., 1973] Crapper, G., Dombrowski, N., Jepson, W., and Pyott, G. (1973). A note on the growth of kelvin-helmholtz waves on thin liquid sheets. *Journal of Fluid Mechanics*, 57(04):671–672.

[Crapper et al., 1975] Crapper, G., Dombrowski, N., and Pyott, G. (1975). Kelvin–helmholtz wave growth on cylindrical sheets. *Journal of Fluid Mechanics*, 68(03):497–502.

[D'albe and Hidayetulla, 1955] D'albe, E. and Hidayetulla, M. (1955). The breakup of large water drops falling at terminal velocity in free air. *Quarterly Journal of the Royal Meteorological Society*, 81(350):610–613.

[De Luca and Costa, 1997] De Luca, L. and Costa, M. (1997). Instability of a spatially developing liquid sheet. *Journal of Fluid Mechanics*, 331:127–144.

[Drazin and Reid,] Drazin, P. and Reid, W. Hydrodynamic stability, 1981. *Cambridge U. Press, Cambridge*.

[Duan et al., 2003] Duan, R.-Q., Koshizuka, S., and Oka, Y. (2003). Numerical and theoretical investigation of effect of density ratio on the critical weber number of droplet breakup. *Journal of nuclear science and technology*, 40(7):501–508.

[Durst and Zaré, 1976] Durst, F. and Zaré, M. (1976). Laser doppler measurements in two-phase flows. In *The accuracy of flow measurements by laser Doppler methods*, volume 1, pages 403–429.

[Eggers and Villermaux, 2008] Eggers, J. and Villermaux, E. (2008). Physics of liquid jets. *Reports on progress in physics*, 71(3):036601.

[Faeth,] Faeth, G. Structure and atomization properties of dense turbulent sprays. In *Symposium (International) on Combustion*, volume 23, pages 1345–1352. Elsevier.

[Faeth et al., 1995] Faeth, G., Hsiang, L.-P., and Wu, P.-K. (1995). Structure and breakup properties of sprays. *International Journal of Multiphase Flow*, 21:99–127.

[Feng and Beard, 1991] Feng, J. Q. and Beard, K. V. (1991). A perturbation model of raindrop oscillation characteristics with aerodynamic effects. *Journal of the atmospheric sciences*, 48(16):1856–1868.

[Gelfand, 1996] Gelfand, B. (1996). Droplet breakup phenomena in flows with velocity lag. *Progress in Energy and Combustion Science*, 22(3):201–265.

[Gordon, 1959] Gordon, G. (1959). Mechanism and speed of breakup of drops. *Journal of Applied Physics*, 30(11):1759–1761.

[Guildenbecher et al., 2009] Guildenbecher, D., López-Rivera, C., and Sojka, P. (2009). Secondary atomization. *Experiments in Fluids*, 46(3):371–402.

[Hagerty and Shea, 1955] Hagerty, W. and Shea, J. (1955). A study of the stability of plane fluid sheets. *J. Appl. Mech*, 22(3):509–514.

[Harper et al., 1972] Harper, E., Grube, G., and Chang, I.-D. (1972). On the breakup of accelerating liquid drops. *Journal of Fluid Mechanics*, 52(03):565–591.

[Hinze, 1949] Hinze, J. (1949). Critical speeds and sizes of liquid globules. *Applied Scientific Research*, 1(1):273–288.

[Hinze, 1955] Hinze, J. (1955). Fundamentals of the hydrodynamic mechanism of splitting in dispersion processes. *AIChE Journal*, 1(3):289–295.

[Hsiang and Faeth, 1993a] Hsiang, L. and Faeth, G. (1993a). Deformation and secondary breakup of drops. *AIAA Paper*, (93-0814).

[Hsiang and Faeth, 1992a] Hsiang, L. and Faeth, M. (1992a). Secondary drop breakup in the deformation regime. *Ann Arbor*, 1001:48109–2140.

[Hsiang and Faeth, 1992b] Hsiang, L.-P. and Faeth, G. M. (1992b). Near-limit drop deformation and secondary breakup. *International Journal of Multiphase Flow*, 18(5):635–652.

[Hsiang and Faeth, 1993b] Hsiang, L.-P. and Faeth, G. M. (1993b). Drop properties after secondary breakup. *International Journal of Multiphase Flow*, 19(5):721–735.

[Hwang et al., 1996] Hwang, S., Liu, Z., and Reitz, R. D. (1996). Breakup mechanisms and drag coefficients of high-speed vaporizing liquid drops. *Atomization and Sprays*, 6(3).

[Ibrahim and Jog, 2008] Ibrahim, A. and Jog, M. (2008). Nonlinear instability of an annular liquid sheet exposed to gas flow. *International Journal of Multiphase Flow*, 34(7):647–664.

[Ibrahim et al., 2006] Ibrahim, A., Jog, M. A., and Jeng, S. (2006). Effect of liquid swirl-velocity profile on the instability of a swirling annular liquid sheet. *Atomization and sprays*, 16(3).

[Ibrahim and Jog, 2006] Ibrahim, A. A. and Jog, M. A. (2006). Effect of liquid and air swirl strength and relative rotational direction on the instability of an annular liquid sheet. *Acta mechanica*, 186(1-4):113–133.

[Ibrahim et al., 1993] Ibrahim, E., Yang, H., and Przekwas, A. (1993). Modeling of spray droplets deformation and breakup. *Journal of Propulsion and Power*, 9(4):651–654.

[Jazayeri and Li, 2000] Jazayeri, S. A. and Li, X. (2000). Nonlinear instability of plane liquid sheets. *Journal of Fluid Mechanics*, 406:281–308.

[Jeandel and Dumouchel, 1999] Jeandel, X. and Dumouchel, C. (1999). Influence of the viscosity on the linear stability of an annular liquid sheet. *International journal of heat and fluid flow*, 20(5):499–506.

[Jiang et al., 1992] Jiang, Y., Umemura, A., and Law, C. (1992). An experimental investigation on the collision behaviour of hydrocarbon droplets. *Journal of Fluid Mechanics*, 234:171–190.

[Joseph et al., 1999] Joseph, D. D., Belanger, J., and Beavers, G. (1999). Breakup of a liquid drop suddenly exposed to a high-speed airstream. *International Journal of Multiphase Flow*, 25(6):1263–1303.

[Kaario et al., 2002] Kaario, O., Larmi, M., and Tanner, F. (2002). Non-evaporating liquid spray simulations with the etab and wave droplet breakup models. *Zaragoza*, 9:11.

[Koenig, 1965] Koenig, L. R. (1965). Drop freezing through drop breakup. *Journal of the Atmospheric Sciences*, 22(4):448–451.

[Kull, 1991] Kull, H.-J. (1991). Theory of the rayleigh-taylor instability. *Physics Reports*, 206(5):197–325.

[Lading and Andersen, 1989] Lading, L. and Andersen, K. (1989). Estimating frequency and phase for velocity and size measurements [laser anemometry]. In *Instrumentation in Aerospace Simulation Facilities, 1989. ICIASF'89 Record., International Congress on*, pages 274–290.

[Lamb, 1993] Lamb, H. (1993). *Hydrodynamics*. Cambridge university press.

[LeClair et al., 1972] LeClair, B., Hamielec, A., Pruppacher, H., and Hall, W. (1972). A theoretical and experimental study of the internal circulation in water drops falling at terminal velocity in air. *Journal of the Atmospheric Sciences*, 29(4):728–740.

[Lee and Reitz, 2000] Lee, C. and Reitz, R. D. (2000). An experimental study of the effect of gas density on the distortion and breakup mechanism of drops in high speed gas stream. *International journal of multiphase flow*, 26(2):229–244.

[Lee and Park, 2002] Lee, C. S. and Park, S. W. (2002). An experimental and numerical study on fuel atomization characteristics of high-pressure diesel injection sprays. *Fuel*, 81(18):2417–2423.

[Lee et al., 2013] Lee, J., Basu, S., and Kumar, R. (2013). Comparison and cross-validation of optical techniques in different swirl spray regimes. *Atomization and Sprays*, 23(8).

[Lee et al., 2012] Lee, M. W., Park, J. J., Farid, M. M., and Yoon, S. S. (2012). Comparison and correction of the drop breakup models for stochastic dilute spray flow. *Applied Mathematical Modelling*, 36(9):4512–4520.

[Li and Tankin, 1991] Li, X. and Tankin, R. (1991). On the temporal instability of a two-dimensional viscous liquid sheet. *Journal of Fluid Mechanics*, 226:425–443.

[Lienemann et al., 2007] Lienemann, H., Shrimpton, J., and Fernandes, E. (2007). A study on the aerodynamic instability of attenuating liquid sheets. *Experiments in fluids*, 42(2):241–258.

[Lin and Jiang, 2003] Lin, S. and Jiang, W. (2003). Absolute and convective instability of a radially expanding liquid sheet. *Physics of Fluids (1994-present)*, 15(6):1745–1754.

[Lin and Lian, 1990] Lin, S. and Lian, Z. (1990). Mechanisms of the breakup of liquid jets. *AIAA Journal*, 28(1):120–126.

[Lin et al., 1990] Lin, S., Lian, Z., and Creighton, B. (1990). Absolute and convective instability of a liquid sheet. *Journal of Fluid Mechanics*, 220:673–689.

[Lin and Reitz, 1998] Lin, S. and Reitz, R. (1998). Drop and spray formation from a liquid jet. *Annual Review of Fluid Mechanics*, 30(1):85–105.

[Lin, 2003] Lin, S.-P. (2003). *Breakup of liquid sheets and jets*, volume 120. Cambridge University Press Cambridge, England.

[Liu et al., 1993] Liu, A. B., Mather, D., and Reitz, R. D. (1993). Modeling the effects of drop drag and breakup on fuel sprays. Report, SAE Technical Paper.

[Liu and Reitz, 1997] Liu, Z. and Reitz, R. (1997). An analysis of the distortion and breakup mechanisms of high speed liquid drops. *International journal of multiphase flow*, 23(4):631–650.

[Luna and Klikoff Jr, 1967] Luna, R. and Klikoff Jr, W. (1967). Aerodynamic breakup of liquid drops. Report, Sandia Corp., Albuquerque, N. Mex.

[Mansour and Chigier, 1990] Mansour, A. and Chigier, N. (1990). Disintegration of liquid sheets. *Physics of Fluids A: Fluid Dynamics (1989-1993)*, 2(5):706–719.

[Mansour and Chigier, 1991] Mansour, A. and Chigier, N. (1991). Dynamic behavior of liquid sheets. *Physics of Fluids A: Fluid Dynamics (1989-1993)*, 3(12):2971–2980.

[Marmottant and Villermaux, 2004a] Marmottant, P. and Villermaux, E. (2004a). Fragmentation of stretched liquid ligaments. *Physics of Fluids (1994-present)*, 16(8):2732–2741.

[Marmottant and Villermaux, 2004b] Marmottant, P. and Villermaux, E. (2004b). On spray formation. *Journal of fluid mechanics*, 498:73–111.

[Martin and Meiburg, 1994] Martin, J. and Meiburg, E. (1994). On the stability of the swirling jet shear layer. *Physics of Fluids (1994-present)*, 6(1):424–426.

[Martin and Meiburg, 1996] Martin, J. and Meiburg, E. (1996). Nonlinear axisymmetric and threedimensional vorticity dynamics in a swirling jet model. *Physics of Fluids (1994-present)*, 8(7):1917–1928.

[Martin and Meiburg, 1991] Martin, J. E. and Meiburg, E. (1991). Numerical investigation of three-dimensionally evolving jets subject to axisymmetric and azimuthal perturbations. *Journal of Fluid Mechanics*, 230:271–318.

[Mehring and Sirignano, 1999] Mehring, C. and Sirignano, W. (1999). Nonlinear capillary wave distortion and disintegration of thin planar liquid sheets. *Journal of Fluid Mechanics*, 388:69–113.

[Mehring and Sirignano, 2000a] Mehring, C. and Sirignano, W. (2000a). Axisymmetric capillary waves on thin annular liquid sheets. i. temporal stability. *Physics of Fluids (1994-present)*, 12(6):1417–1439.

[Mehring and Sirignano, 2000b] Mehring, C. and Sirignano, W. (2000b). Axisymmetric capillary waves on thin annular liquid sheets. ii. spatial development. *Physics of Fluids (1994-present)*, 12(6):1440–1460.

[Mehring and Sirignano, 2001] Mehring, C. and Sirignano, W. A. (2001). Nonlinear capillary waves on swirling, axisymmetric free liquid films. *International journal of multiphase flow*, 27(10):1707–1734.

[Mehring and Sirignano, 2004] Mehring, C. and Sirignano, W. A. (2004). Capillary stability of modulated swirling liquid sheets. *Atomization and Sprays*, 14(5).

[Opfer et al., 2014] Opfer, L., Roisman, I., Venzmer, J., Klostermann, M., and Tropea, C. (2014). Droplet-air collision dynamics: Evolution of the film thickness. *Physical Review E*, 89(1):013023.

[O'Rourke and Amsden, 1987] O'Rourke, P. J. and Amsden, A. A. (1987). The tab method for numerical calculation of spray droplet breakup. Report, SAE Technical Paper.

[Park et al., 2002] Park, J.-H., Yoon, Y., and Hwang, S.-S. (2002). Improved tab model for prediction of spray droplet deformation and breakup. *Atomization and Sprays*, 12(4).

[Park et al., 2009] Park, S. H., Kim, H. J., Suh, H. K., and Lee, C. S. (2009). Experimental and numerical analysis of spray-atomization characteristics of biodiesel fuel in various fuel and ambient temperatures conditions. *International journal of heat and fluid flow*, 30(5):960–970.

[Pilch and Erdman, 1987] Pilch, M. and Erdman, C. (1987). Use of breakup time data and velocity history data to predict the maximum size of stable fragments for acceleration-induced breakup of a liquid drop. *International Journal of Multiphase Flow*, 13(6):741–757.

[Qian and Law, 1997] Qian, J. and Law, C. (1997). Regimes of coalescence and separation in droplet collision. *Journal of Fluid Mechanics*, 331:59–80.

[Rangel and Sirignano, 1988] Rangel, R. and Sirignano, W. (1988). Nonlinear growth of kelvin–helmholtz instability: effect of surface tension and density ratio. *Physics of Fluids (1958-1988)*, 31(7):1845–1855.

[Rangel and Sirignano, 1991] Rangel, R. and Sirignano, W. (1991). The linear and nonlinear shear instability of a fluid sheet. *Physics of Fluids A: Fluid Dynamics (1989-1993)*, 3(10):2392–2400.

[Ranger and Nicholls, 1969] Ranger, A. A. and Nicholls, J. (1969). Aerodynamic shattering of liquid drops. *Aiaa Journal*, 7(2):285–.

[Rayleigh,] Rayleigh, L. On the capillary phenomena of jets. In *Proc. R. Soc. London*, volume 29, pages 71–97.

[Rayleigh, 1879] Rayleigh, L. (1879). On the stability, or instability, of certain fluid motions. *Proceedings of the London Mathematical Society*, 1(1):57–72.

[Reitz and Bracco, 1982] Reitz, R. and Bracco, F. (1982). Mechanism of atomization of a liquid jet. *Physics of Fluids (1958-1988)*, 25(10):1730–1742.

[Reitz and Diwakar, 1986] Reitz, R. D. and Diwakar, R. (1986). Effect of drop breakup on fuel sprays. Report, SAE Technical Paper.

[Rimbert and Castanet, 2011] Rimbert, N. and Castanet, G. (2011). Crossover between rayleigh-taylor instability and turbulent cascading atomization mechanism in the bag-breakup regime. *Physical Review E*, 84(1):016318.

[Rizk and Lefebvre, 1985] Rizk, N. and Lefebvre, A. H. (1985). Internal flow characteristics of simplex swirl atomizers. *Journal of Propulsion and Power*, 1(3):193–199.

[Saha et al., 2012] Saha, A., Lee, J. D., Basu, S., and Kumar, R. (2012). Breakup and coalescence characteristics of a hollow cone swirling spray. *Physics of Fluids (1994-present)*, 24(12):124103.

[Senecal et al., 1999] Senecal, P., Schmidt, D. P., Nouar, I., Rutland, C. J., Reitz, R. D., and Corradini, M. (1999). Modeling high-speed viscous liquid sheet atomization. *International Journal of Multiphase Flow*, 25(6):1073–1097.

[Shraiber et al., 1996] Shraiber, A., Podvysotsky, A., and Dubrovsky, V. (1996). Deformation and breakup of drops by aerodynamic forces. *Atomization and Sprays*, 6(6).

[Sirignano and Mehring, 2000] Sirignano, W. and Mehring, C. (2000). Review of theory of distortion and disintegration of liquid streams. *Progress in Energy and Combustion Science*, 26(4):609–655.

[Squire, 1953] Squire, H. (1953). Investigation of the instability of a moving liquid film. *British Journal of Applied Physics*, 4(6):167.

[Stone, 1994] Stone, H. A. (1994). Dynamics of drop deformation and breakup in viscous fluids. *Annual Review of Fluid Mechanics*, 26(1):65–102.

[Stone et al., 1986] Stone, H. A., Bentley, B., and Leal, L. (1986). An experimental study of transient effects in the breakup of viscous drops. *Journal of Fluid Mechanics*, 173:131–158.

[Stone and Leal, 1989] Stone, H. A. and Leal, L. (1989). Relaxation and breakup of an initially extended drop in an otherwise quiescent fluid. *Journal of Fluid Mechanics*, 198:399–427.

[Strutt and Rayleigh, 1878] Strutt, J. W. and Rayleigh, L. (1878). On the instability of jets. *Proc. London Math. Soc*, 10:4–13.

[Tanner, 2004] Tanner, F. X. (2004). Development and validation of a cascade atomization and drop breakup model for high-velocity dense sprays. *Atomization and sprays*, 14(3).

[Taylor, 1959a] Taylor, G. (1959a). The dynamics of thin sheets of fluid. ii. waves on fluid sheets. *Proceedings of the Royal Society of London. Series A. Mathematical and Physical Sciences*, 253(1274):296–312.

[Taylor, 1959b] Taylor, G. (1959b). The dynamics of thin sheets of fluid. iii. disintegration of fluid sheets. *Proceedings of the Royal Society of London. Series A. Mathematical and Physical Sciences*, 253(1274):313–321.

[Taylor, 1963] Taylor, G. (1963). The shape and acceleration of a drop in a high speed air stream.

[Taylor and Howarth, 1959] Taylor, G. and Howarth, L. (1959). The dynamics of thin sheets of fluid. i. water bells. *Proceedings of the Royal Society of London. Series A. Mathematical and Physical Sciences*, 253(1274):289–295.

[Theofanous, 2011] Theofanous, T. (2011). Aerobreakup of newtonian and viscoelastic liquids. *Annual Review of Fluid Mechanics*, 43:661–690.

[Theofanous and Li, 2008] Theofanous, T. and Li, G. (2008). On the physics of aerobreakup. *Physics of Fluids (1994-present)*, 20(5):052103.

[Theofanous et al., 2004] Theofanous, T., Li, G., and Dinh, T.-N. (2004). Aerobreakup in rarefied supersonic gas flows. *Journal of fluids engineering*, 126(4):516–527.

[Theofanous et al., 2007] Theofanous, T., Li, G., Dinh, T.-N., and Chang, C.-H. (2007). Aerobreakup in disturbed subsonic and supersonic flow fields. *Journal of Fluid Mechanics*, 593:131–170.

[Villermaux, 2007] Villermaux, E. (2007). Fragmentation. *Annu. Rev. Fluid Mech.*, 39:419–446.

[Villermaux and Clanet, 2002] Villermaux, E. and Clanet, C. (2002). Life of a flapping liquid sheet. *Journal of fluid mechanics*, 462:341–363.

[Villermaux et al., 2004] Villermaux, E., Marmottant, P., and Duplat, J. (2004). Ligament-mediated spray formation. *Physical review letters*, 92(7):074501.

[Wang et al., 2008] Wang, Y., Im, K.-S., and Fezzaa, K. (2008). Similarity between the primary and secondary air-assisted liquid jet breakup mechanisms. *Physical review letters*, 100(15):154502.

[Wei and Yong, 2014] Wei, X. and Yong, H. (2014). Improved semiempirical correlation to predict sauter mean diameter for pressure-swirl atomizers. *Journal of Propulsion and Power*, 30(6):1628–1635.

[Weihs, 1978] Weihs, D. (1978). Stability of thin, radially moving liquid sheets. *Journal of Fluid Mechanics*, 87(02):289–298.

[Whitham, 2011] Whitham, G. B. (2011). *Linear and nonlinear waves*, volume 42. John Wiley & Sons.

[Wierzba, 1990] Wierzba, A. (1990). Deformation and breakup of liquid drops in a gas stream at nearly critical weber numbers. *Experiments in Fluids*, 9(1-2):59–64.

[Wierzba and Takayama, 1988] Wierzba, A. and Takayama, K. (1988). Experimental investigation of the aerodynamic breakup of liquid drops. *AIAA journal*, 26(11):1329–1335.

[Williams, 1958] Williams, F. (1958). Spray combustion and atomization. *Physics of Fluids (1958-1988)*, 1(6):541–545.

[Zhao et al., 2014] Zhao, H., Liu, H.-F., Tian, X.-S., Xu, J.-L., Li, W.-F., and Lin, K.-F. (2014). Outer ligament-mediated spray formation of annular liquid sheet by an inner round air stream. *Experiments in Fluids*, 55(8):1–13.